International Journal of Mechanical Sciences 293 (2025) 110144

Contents lists available at ScienceDirect

International Journal of Mechanical Sciences

journal homepage: www.elsevier.com/locate/ijmecsci

Observation of multi-type corner states in right-angled trapezoidal sonic crystals

Tao Yang [a,b], Qian Wu [c], Shaoyun Wang [c], Rongyao Wei [b], Yu Liu [b], Quan Wang [d], Heng Jiang [a,b,*], Guoliang Huang [e,*]

[a] Wide Range Flight Engineering Science and Applications Center, Institute of Mechanics, Chinese Academy of Sciences, Beijing, 100190, China
[b] Key Laboratory of Microgravity, Institute of Mechanics, Chinese Academy of Sciences, Beijing, 100190, China
[c] Department of Mechanical and Aerospace Engineering, University of Missouri, Columbia, MO 65211, United States of America
[d] Department of Civil and Environmental Engineering, Shantou University, Shantou, 515063, China
[e] Department of Mechanics and Engineering Science, Peking University, Beijing, 100871, China

ARTICLE INFO

Keywords:
Higher-order topological insulators
Sonic crystal
Topological corner states
Wannier bands
Glide symmetry
Right-angled trapezoidal

ABSTRACT

Previous research has demonstrated corner states with various angular types through distinct structural configurations. However, achieving multiple corner state types within a single lattice has remained elusive. This study addresses the challenge in realizing multi-type corner states within a unified lattice design by introducing a novel right-angled trapezoidal topological sonic crystal. We propose a two-dimensional C-shaped square-lattice unit cell with $p4gg$ symmetry, which facilitates the realization of topological quadrupoles without relying on tight-binding mechanisms. The topological properties within the quadrupole topological band gap are confirmed through Wannier band and nested Wannier band calculations, with the location of Wannier centers accurately predicting the distribution of edge and corner states. To illustrate this, we construct both square-shaped and right-angled trapezoidal sonic crystals with a unified lattice design. Unlike the square-shaped structure, the trapezoidal design supports multi-type corner states at distinct frequencies, accommodating obtuse, right, and acute angles. An additional in-gap hypotenuse edge state underscores the versatility of this design. Experimental results validate these theoretical predictions, offering concrete evidence of multi-type corner states and their unique behaviors. This innovative approach not only simplifies the realization of topological quadrupoles but also opens new avenues for applications in acoustic wave control, energy harvesting, and precise sound manipulation.

1. Introduction

The discovery of topological insulators (TIs) [1,2] has significantly expanded the boundaries of condensed matter physics. TIs introduce a new framework with their unique ability to support robust boundary transmission. This groundbreaking concept has gained considerable attention across various fields, including electronics, photonics, mechanics, and acoustics. Research on TIs has delved into multiple quantum phenomena, such as the quantum Hall effect [3,4], the quantum spin Hall effect [5,6], and the quantum valley Hall effect [7,8]. These phenomena are typically characterized by quantized dipole moments that give rise to $(d-1)$-dimensional topological surface or edge states in d-dimensional TIs.

The bulk-boundary correspondence principle, first associated with conventional TIs, has since been extended to higher-order topological insulators (HOTIs) [9–14]. This has led to the discovery of more complex topological states. In a d-dimensional system, an nth-order TI gives rise to $(d-n)$-dimensional edge states, where $1 < n \leq d$. For example, in a two-dimensional (2D) second-order TI, not only gapped one-dimensional (1D) edge states but also in-gap zero-dimensional (0D) corner states can appear. This allows for greater control of energy flow compared to traditional 2D TIs. These 2D second-order TIs derive their topological properties from a quantized quadrupole moment, a concept initially introduced in electronic systems. Recently, several HOTI models, such as the Benalcazar–Bernevig–Hughes model [15,16] and the kagome model [17–19], have been developed. However, these models rely heavily on crystal symmetry, making it difficult to realize HOTIs in electronic systems due to the complexities involved in synthesizing ideal materials.

On the other hand, acoustic artificial lattices, such as metamaterials and phononic crystals, offer significant potential for realizing acoustic TIs, thanks to the design flexibility of their artificial structures.

* Corresponding authors.
E-mail addresses: hengjiang@imech.ac.cn (H. Jiang), guohuang@pku.edu.cn (G. Huang).

https://doi.org/10.1016/j.ijmecsci.2025.110144
Received 14 December 2024; Received in revised form 24 February 2025; Accepted 11 March 2025
Available online 27 March 2025

In recent years, advances in acoustic TIs have garnered significant attention due to their potential for various applications in sound manipulation, such as noise control [20–22], non-destructive testing [23–25], and acoustic waveguiding [26–28]. Researchers have explored numerous innovative designs based on engineered metamaterials and phononic crystals, including quantum Hall-like effect that leverage breaking time-reversal symmetry [29–32], quantum spin Hall-like effect that features pseudo-spin degrees of freedom [33–36], quantum valley Hall-like effect that showcase valley degree of freedom [37–41], and non-Hermitian topological phases [42–45]. In acoustic systems, researchers have successfully observed corner states in HOTIs, even before their electronic counterparts. To realize acoustic HOTIs, a variety of strategies have been explored [46–56]. One approach that have been extensively studied is to embed low-dimensional TIs into HOTIs using the generalized Su-Schrieffer-Heeger (SSH) model, which can take various forms, such as 2D SSH lattices [57–59], square-root models [60–62], and synthetic dimensions [63–66]. Another approach involves using the Jackiw-Rebbi soliton mechanism to break the symmetry of gapless edge states [67–71]. Recent advancements in three-dimensional (3D) acoustic TIs have further broadened our understanding of HOTIs, revealing novel topological states such as 2D surface states, 1D hinge states, and 0D corner states [72–75].

Designing 2D HOTIs, however, often requires tight-binding mechanisms and specific crystalline symmetries, such as C_4 [48,76] and C_6 [77–80], which place constraints on rotational symmetries within the unit cell. Achieving fractional corner charge typically involves combining topologically trivial and non-trivial structures [81,82], or fine-tuning intercellular and intracellular couplings [43,81], adding complexity to the structural design. Additionally, generating corner modes often requires constructing sonic crystal (SC) with specific polygonal shapes, which can force the higher-order topological states to be located at the specific corners. Recent studies have reported various types of corner states, including acute-angled and obtuse-angled states in kagome lattices [19,83], as well as right-angled [82,84] and straight-angled states [85] in square lattices. However, designing and experimentally validating multi-type corner states within a single lattice structure remains a challenge, highlighting gaps in our understanding of these complex topological systems.

Recently, the $p4g$ wallpaper symmetry has been studied by the Ref. [86], enabling a hierarchy of topological multipoles in sonic crystals. The cited study demonstrates that glide symmetry alone can quantize higher-order topological invariants. Specifically, the lowest band gap exhibits a quantized Wannier dipole topology, mimicking the quantum spin Hall effect, while the second band gap features an anomalous quadrupole topology, characterized by gapped Wannier bands and distinct edge and corner states. These states are experimentally observed in a square sonic crystals composed exclusively of right-angle (90°) corners. However, the corner states in irregular lattices that incorporate both conventional right angles and non-right angles, including those exceeding 180° has not been explored. While the study employs Wannier bands to infer topological quadrupole moments, it does not provide explicit Wannier center distributions, which are crucial for predicting corner states in generalized geometries.

To address this gap, we systematically employs Wannier center analysis, to rigorously characterize the corner states in irregular geometry. We develop a generalized predictive framework based on Wannier center distributions under $p4gg$ symmetry, enabling us to map the positions of Wannier centers to the emergence of corner states for any arbitrary angle. This approach allows us to predict corner states in geometries with angles larger than 90°, such as 135°, 225°, 270°, and 315°. We present a 2D C-shaped square-lattice unit cell with $p4gg$ symmetry. constructed to meet non-degenerate Wannier band criteria, preserving fourfold rotational symmetry and enforcing glide symmetries along the x- and y-directions. To eliminate mirror symmetry and amplify chirality, we employ C-shaped scatterers with two critical modifications: 1. The center of mass is shifted from the quarter-unit cell centroid to enhance polarization. 2. The connector segment between C-scatterer arms is engineered with distinct thickness. This design enables the realization of topological quadrupoles without relying on tight-binding mechanisms. The second band gap (the second lowest) of this crystal shows nontrivial quadrupole topological properties protected by glide symmetry. These properties are confirmed through Wannier band and nested Wannier band calculations. By analyzing the modes at high-symmetry points, we determine the Wannier center location within the unit cell, allowing us to predict the formation and distribution of corner states. Based on this analysis, we construct two SCs: a square-shaped SC and a right-angled trapezoidal SC. The distribution of corner states is verified through eigenmode, Wannier center, and density of states (DOS) analyses. In the right-angled trapezoidal SC, corner states appear at specific frequencies with varying angular distributions, including obtuse, right, and acute angles, and some hypotenuse edge states also appear within the band gap. As the cutting boundary of SC changes, the acute and obtuse corner states disappear, reflecting shifts in the Wannier center location. To validate these findings, we fabricate a right-angled trapezoidal SC sample using 3D printing and experimentally confirm the existence of corner states predicted. This structure not only allows for diverse corner states in HOTIs, but also simplifies the manufacturing process, making it promising for future applications.

This paper is organized as follows. Section 2 presents the acoustic topological model, detailing the design of the $p4gg$ symmetric unit cell and the calculation of Wannier bands and nested Wannier bands using the Wilson loop method to analyze the topological properties of the band gaps. Section 3 focuses on the characterization of edge and corner states in a square-shaped sonic crystal, validating the theoretical predictions through eigenmode and DOS analyses. Section 4 investigates the presence and robustness of multi-type corner states, including acute, obtuse, and right angles, in a right-angled trapezoidal sonic crystal, supported by experimental measurements. Section 5 concludes the study, summarizing the key findings and highlighting their implications for future applications in topological acoustics and advanced wave control technologies. Appendices provide additional technical details, including the calculation process for Wannier bands and the influence of loss factors on transmission spectra.

2. Unit cell design and wannier center configuration

In this section, we present the design of the unit cell possessing $p4gg$ symmetry tailored for realizing a HOTI and systematically investigate its associated topological properties. Our focus centers on the topological characteristics of band gaps. By analyzing the Wannier bands and their nested counterparts, we classify the first band gap—the lowest in energy—as topologically trivial. In contrast, the second band gap is identified as a quadrupole topological band gap, indicative of higher-order topology. Using detailed modal analysis, we establish the configuration of Wannier centers within the unit cell. These centers are localized precisely at the lattice points, reflecting the symmetry and topology of the system. The combination of the bandgap topology and the spatial distribution of the Wannier centers enables us to predict the emergence of bulk, edge, and corner states. These findings not only confirm the theoretical framework underlying the system's topology but also serve as the foundation for the subsequent development of this work.

The proposed SC is made from photosensitive resin (mass density $\rho = 1.3\,\mathrm{g/cm^3}$, modulus $B = 2765\,\mathrm{MPa}$), as shown in Fig. 1(a). This material serves as a sound-hard boundary compared to the background air medium (mass density $\rho = 1.29\,\mathrm{kg/m^3}$, sound velocity $c = 343\,\mathrm{m/s}$). The unit cell of the SC, shown in Fig. 1(b), contains four identical C-shaped scatterers (blue areas) arranged within an air medium (white area). It exhibits $p4gg$ symmetry, with four-fold rotational symmetry and glide symmetry along both the x- and y-axes: $G_x = (x, y) \rightarrow (a/2 + x, a/2 - y)$ and $G_y = (x, y) \rightarrow (a/2 - x, a/2 + y)$. By employing the

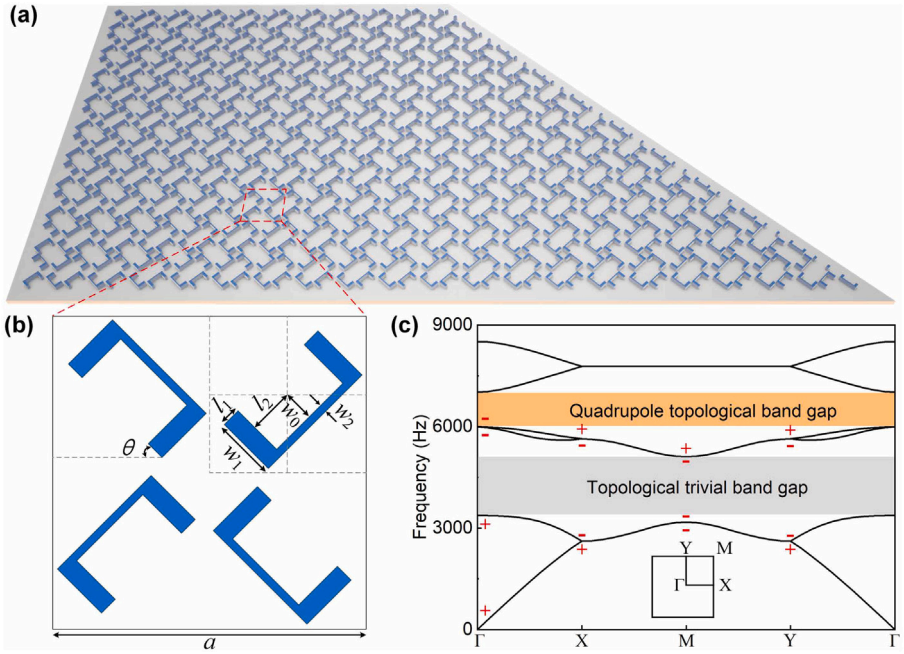

Fig. 1. 2D right-angled trapezoidal SC with unit cell design and its band structure. (a) Schematic of the 2D right-angled trapezoidal SC proposed in this work. (b) Unit cell of the SC, consisting of four identical C-shaped scatterers. The lattice constant is $a = 4$ cm, and the geometric parameters of the scatterers are: $w_0 = 0.4$ cm, $w_1 = 0.1$ cm, $w_2 = 0.25$ cm, $l_1 = 0.8$ cm, and $l_2 = 1.2$ cm. Each scatterer is oriented at an angle of $\theta = 45°$ relative to the horizontal axis. (c) Acoustic band structures of the SC, with the BZ shown in the inset. Symbols +/− label even/odd parities at the Γ, X, M, and Y points, respectively.

commercial software COMSOL Multiphysics, the acoustic band structures of the SC is derived by scanning the wave vector along the path Γ-X-M-Y-Γ in the first Brillouin zone (BZ), as shown in Fig. 1(c). The glide symmetry of the unit cell results in doubly degenerate dispersion curves along the XM boundary of the BZ, while the C_4 symmetry leads to double degeneracy along the YM line. Two band gaps are observed, each representing different topological characteristics. These topological properties can be analyzed through Wannier bands and nested Wannier bands.

To obtain the Wannier bands, we compute the Wilson loop operator matrix for the lower acoustic bands below the relevant band gap. This process allows for a detailed analysis of the band gap's topological properties and a deeper understanding of its behavior [87–89]. According to the Bloch theorem, the wave function $|u_{n,\boldsymbol{k}}\rangle$ takes the form

$$|u_{n,\boldsymbol{k}}\rangle = e^{-\mathrm{i}\boldsymbol{k}\boldsymbol{r}}|P_{n,\boldsymbol{k}}\rangle, \tag{1}$$

where $\mathrm{i}^2 = -1$, $\boldsymbol{r}$ represents the position vector, $\boldsymbol{k}$ denotes the wave vector, and $|P_{n,\boldsymbol{k}}\rangle$ represents the sound pressure field. Here, n=1…N denotes the acoustic band index, with N signifying the total number of bands below the band gap of interest. For the first band gap, $N = 2$ and for the second band gap, $N = 4$. We consider the Wilson loop operator along the x direction $W_{x,(k_x+\frac{2\pi}{a},k_y)\leftarrow(k_x,k_y)}$ and take the (k_x, k_y) as the starting point of the loop. The calculation process for the Wilson loop is detailed in Appendix A. The Wilson loop for the proposed unit cell is obtained as

$$W_{x,(k_x+\frac{2\pi}{a},k_y)\leftarrow(k_x,k_y)}(k_y) = \prod_{j=0}^{N_x-1} F_{x,\boldsymbol{k}+j\Delta k_x}, \tag{2}$$

where $\Delta k_x = \frac{2\pi}{N_x a}$, with N_x representing the number of discrete k_x points, here we take $N_x = 30$. $F_{x,\boldsymbol{k}}$ is an $N \times N$ matrix, and each of its entries can be defined as

$$F^{mn}_{x,\boldsymbol{k}} = \left\langle u_{m,\boldsymbol{k}+\Delta k_x} \middle| u_{n,\boldsymbol{k}} \right\rangle, \tag{3}$$

where $m, n = 1 \ldots N$. The inner product of wave function is defined as

$$\left\langle u_{m,\boldsymbol{k}} \mid u_{n,\boldsymbol{k}'} \right\rangle = \left(N_{m,\boldsymbol{k}} N_{n,\boldsymbol{k}'}\right)^{-\frac{1}{2}} \int d\boldsymbol{r}\, u^*_{m,\boldsymbol{k}}(\boldsymbol{r}) \cdot \frac{1}{2\rho c^2} \cdot u_{n,\boldsymbol{k}'}(\boldsymbol{r}), \tag{4}$$

where ρ and c are the mass density and sound velocity of air, respectively. The integration is performed over the entire unit cell. Additionally, $N_{m,\boldsymbol{k}}$ denotes the normalization factor, which is defined as

$$N_{m,\boldsymbol{k}} = \int d\boldsymbol{r}\, u^*_{m,\boldsymbol{k}}(\boldsymbol{r}) \cdot \frac{1}{2\rho c^2} \cdot u_{m,\boldsymbol{k}}(\boldsymbol{r}). \tag{5}$$

To obtain the Wannier band, the Wilson loop operator matrix is diagonalized by

$$W_{x,(k_x+\frac{2\pi}{a},k_y)\leftarrow(k_x,k_y)}(k_y)|v^l_{x,\boldsymbol{k}}\rangle = e^{\mathrm{i}2\pi v^l_x(k_y)}|v^l_{x,\boldsymbol{k}}\rangle, \tag{6}$$

where $l = 1 \ldots N$ is the Wannier band index and $|v^l_{x,\boldsymbol{k}}\rangle$ is the eigenvector which depends on both the loop and the starting point of the loop. The phase $v^l_x(k_y)$, which depends only on the Wilson loop, is the Wannier center of the acoustic Bloch waves. The Wannier bands for both the first and second band gaps can be determined using Eqs. (1)–(6). The calculation results are displayed in Fig. 2. In Fig. 2(a), the Wannier bands associated with the first band gap, within the region $k_y \in [-\pi/a, \pi/a)$, are gapless, and the winding number across the BZ is zero, indicating that the first band gap is topologically trivial. Conversely, in Fig. 2(b), the Wannier bands corresponding to the second band gap, also within the region $k_y \in [-\pi/a, \pi/a)$, are gapped and nondegenerate. The Wannier bands 1, 2 and Wannier bands 3, 4 display symmetry about $v_x = 0$. This characteristic suggests that the second band gap has a vanishing dipole, which is a necessary condition for the presence of a topological quadrupole.

Subsequently, the edge polarization can be determined through the nested Wilson-loop method (see Appendix A). For the Wannier bands shown in Fig. 2(b), we split them into two Wannier sectors since they are gapped. One Wannier sector is defined as $\mathrm{I} = \left\{ v^l_{x,\boldsymbol{k}} \mid l = 1, 3 \right\}$, and the other as $\mathrm{II} = \left\{ v^l_{x,\boldsymbol{k}} \mid l = 2, 4 \right\}$. We can define the Wannier band basis $|w^l_{x,\boldsymbol{k}}\rangle$ by utilizing the eigenvectors $|v^l_{x,\boldsymbol{k}}\rangle$ of $W_{x,(k_x+\frac{2\pi}{a},k_y)\leftarrow(k_x,k_y)}(k_y)$ and the Bloch wave functions

$$|w^l_{x,\boldsymbol{k}}\rangle = \sum_{n=1}^{N} \left[v^l_{x,\boldsymbol{k}}\right]^n |u_{n,\boldsymbol{k}}\rangle, \tag{7}$$

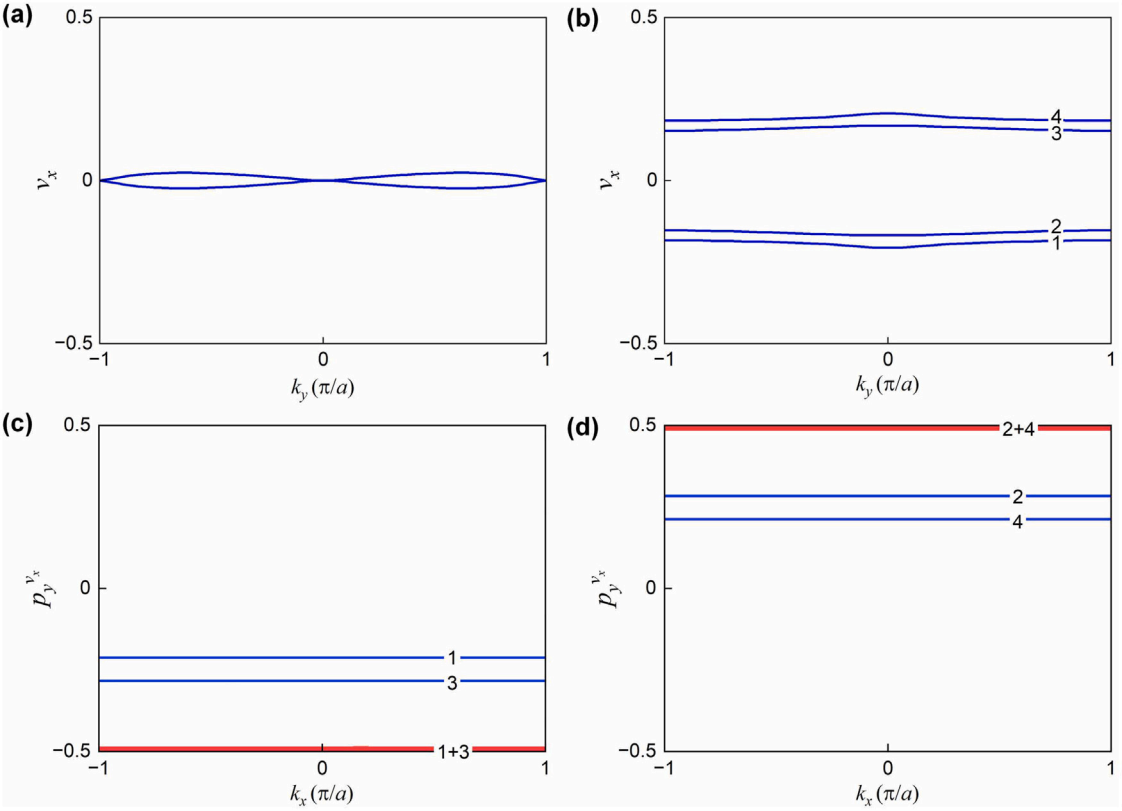

Fig. 2. Wannier bands and nested Wannier bands. (a) Wannier bands for the two acoustic bands below the first band gap. (b) Wannier bands for the four acoustic bands below the second band gap. (c) Nested Wannier bands for the Wannier sector I. (d) Nested Wannier bands for the Wannier sector II.

where $\left[v^l_{x,\boldsymbol{k}}\right]^n$ denotes the nth element of $|v^l_{x,\boldsymbol{k}}\rangle$. Employing this newly established basis, the Wilson loop along y is defined as

$$\tilde{W}_{y,(k_x,k_y+\frac{2\pi}{a})\leftarrow(k_x,k_y)}(k_x)=\prod_{j=0}^{N_y-1}\tilde{F}_{y,\boldsymbol{k}+j\Delta k_y}, \tag{8}$$

where $\Delta k_y = \frac{2\pi}{N_y a}$, with N_y being the number of discrete k_y points, here we take $N_y = 30$. Similarly, each element of matrix $\tilde{F}_{y,\boldsymbol{k}}$ is defined as $\tilde{F}^{mn}_{y,\boldsymbol{k}} = \left\langle w^m_{\boldsymbol{k}+\Delta k_y} \mid w^n_{\boldsymbol{k}}\right\rangle$, where $m,n = 1\ldots N$. To derive the nested Wannier band, the nested Wilson loop matrix is subject to the diagonalization

$$\tilde{W}_{y,(k_x,k_y+\frac{2\pi}{a})\leftarrow(k_x,k_y)}\left(k_x\right)|p^{v_x,l}_{y,\boldsymbol{k}}\rangle = e^{\mathrm{i}2\pi p_y^{v_x,l}(k_x)}|p^{v_x,l}_{y,\boldsymbol{k}}\rangle, \tag{9}$$

where $|p^{v_x,l}_{y,\boldsymbol{k}}\rangle$ is the eigenvector of the nested Wilson loop matrix, and $p_y^{v_x,l}(k_x)$ evolves along k_x forms the nested Wannier bands. Given the distinct separation of Wannier bands, it is feasible to perform the nested Wilson loop calculation for each individual Wannier band. Consequently, this enables the labeling of the nested Wannier bands with their respective Wannier band indices, as depicted in Fig. 2(c) and 2(d). The polarization associated with each Wannier band can be quantitatively expressed as

$$P_y^{v_x,l}=\frac{a}{2\pi}\int dk_x\, p_y^{v_x,l}(k_x). \tag{10}$$

The calculation of Wannier band polarizations for Wannier sectors I and II is undertaken based on the following methodology

$$\begin{aligned} P_y^{v_x,\mathrm{I}} &= \frac{a}{2\pi}\int dk_x\, p_y^{v_x,1}(k_x)+p_y^{v_x,3}(k_x)=-\frac{1}{2},\\ P_y^{v_x,\mathrm{II}} &= \frac{a}{2\pi}\int dk_x\, p_y^{v_x,2}(k_x)+p_y^{v_x,4}(k_x)=\frac{1}{2}. \end{aligned} \tag{11}$$

Given the periodicity of the BZ, which asserts that $P_y^{v_x,\mathrm{I}} = P_y^{v_x,\mathrm{II}} = \frac{1}{2}$, the nontrivial topological quadrupole index that reflects the presence of corner states at the corners of a 2D material is determined by the following calculation

$$q_{xy} = 2P_y^{v_x,\mathrm{I}}P_y^{v_x,\mathrm{II}} = \frac{1}{2} \bmod 1. \tag{12}$$

Based on the above calculated Wannier sector polarization and in light of the literature [90,91], it can be concluded that the Wannier centers of this structure are located at the maximal Wyckoff positions within the unit cell. The maximal Wyckoff positions are the high symmetry points in the real-space unit cell, specifically at the lattice point M and at points X and Y, which lie on the glide-reflection symmetry plane. By computing the eigenmodes of the sound pressure field at the high-symmetry points X, Y, and M (Fig. 3(b)), it is observed that the parities at points X and Y are identical. This indicates that the Wannier centers are positioned on the high symmetry points Γ and M, with none distributed along the glide-reflection symmetry plane, as shown in Fig. 3(a).

3. Demonstration of edge and corner states in a square-shaped sonic crystal

In this section, we characterize the gapped edge states and in-gap corner states using a ribbon-shaped supercell and a square-shaped SC, respectively. Both states are essential features of the quadrupole topological band gap. These results align with the theoretical analysis and validate the predicted distribution of corner states based on Wannier center location. Additionally, by calculating the DOS for the square-shaped SC, we visualize the energy distribution among bulk, edge, and corner states, which further confirms their existence.

First, a ribbon-shaped supercell is constructed, consisting of 10×1 unit cells with a $0.3a$-wide air channel at the boundary, as shown in the inset of Fig. 4(a). Floquet periodic conditions are applied to the top and bottom boundaries, while the sound-hard boundary condition

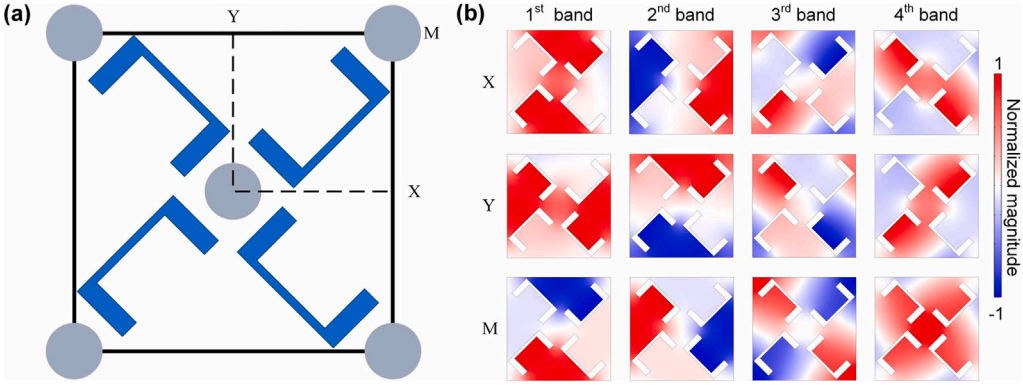

Fig. 3. Wannier center location within the unit cell and eigenmodes at high-symmetry points. (a) Wannier centers (marked by gray dots) within the unit cell. X, Y, and M represent the high-symmetry points in the BZ. (b) Sound pressure field distributions corresponding to the eigenmodes at high-symmetry points X, Y, and M in acoustic bands 1–4.

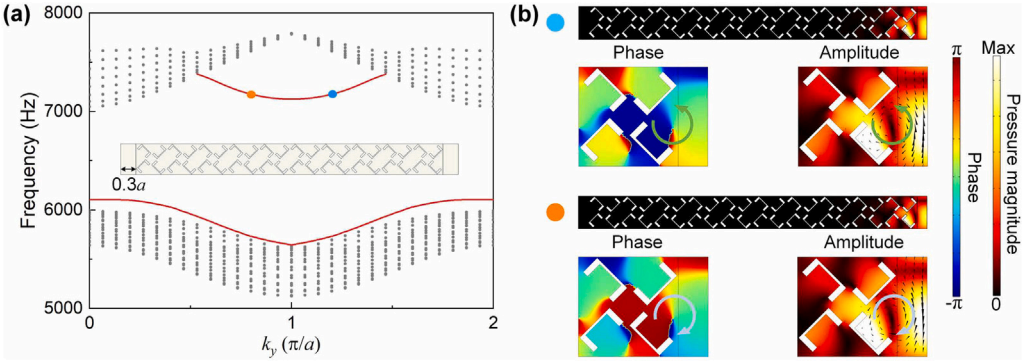

Fig. 4. Topological edge states in the second band gap. (a) Projected band structure of the ribbon-shaped supercell, consisting of 10 × 1 unit cells terminated with a 0.3a-wide air channel (in the k_y direction). The bulk and edge states are marked by gray dots and red curves, respectively. (b) Distributions of phase and amplitude for eigenstate of the edge states at $k_y = 4\pi/5a$ and $k_y = 6\pi/5a$, represented by orange and blue dots, respectively. The energy flow is shown by the black cone arrow, while the white and green arrows indicate the vortex directions in clockwise and counterclockwise orientations.

is imposed on the air channel boundary. The projected band structure of the supercell in the k_y direction around the second band gap is obtained and shown in Fig. 4(a). This structure shows clear features of the quadrupole topological band gap: two edge state curves are gapped, with a quadrupole band gap frequency range of 5995 Hz to 7047 Hz. Additionally, the dispersion curve of the upper edge state overlaps with the bulk acoustic energy band, so that excitation at the frequency of the upper edge state produces a mix of edge and bulk states. Fig. 4(b) shows the phase and sound intensity distribution of the supercell at $k_y = 4\pi/5a$ and $k_y = 6\pi/5a$, represented by orange and blue dots in Fig. 4(a). The simulation results reveal distinct phase and energy flow chiralities, with the pressure field localized at the interface and decaying exponentially into the bulk.

To demonstrate the corner states, we construct a square-shaped SC composed of 10 × 10 unit cells, surrounded by a 0.3a-wide air channel. The cut of the SC is shown in Fig. 5(a), and the boundary of the cut cross the Wannier centers. There exist Wannier centers at all four corner points, indicating the existence of four right-angled corner states in the SC (red dots). Bulk spectrum near the second topological band gap for the SC surrounded by a 0.3a wide air channel, shown in Fig. 5(b), confirms the presence of gapped edge states (blue dots) and in-gap corner states (red dots). These four corner states share the same frequency, 6962 Hz. Due to the overlap in frequency between the upper edge states and bulk states, some edge states falls into the range of bulk states. The sound pressure profiles of the four corner states, shown in Fig. 5(c), reveal that the sound energy is concentrated at the lattice corners and decays rapidly into the bulk.

To visualize the energy distribution of eigenmodes in the square-shaped SC, we analyze the sound field distributions of eigenmodes near the second topological band gap. The eigenmodes are classified into bulk, edge, and corner states. For each type of state, the DOS can be calculated using the following equation from [86]

$$\mathrm{DOS}^j(\omega) = \sum_j \frac{1}{\pi} \frac{\Lambda A_i^j}{(\omega - f_i)^2 + \Lambda^2}, \tag{13}$$

where f_i is the ith eigenfrequency, Λ is the frequency interval width, ω is the frequency interval center, and $A_i^j = E_i^j / E_i^{\mathrm{All}}$ represents the energy share of bulk, edge, or corner states. Here, E_i^j is the integrated sound pressure intensity over the jth region (bulk, edge, or corner), and E_i^{All} is the total sound pressure intensity integrated over the entire SC. Eq. (13) quantifies the density of specific modes within the eigenmode spectrum, offering insights into the dominant acoustic wave transmission modes, especially near the topological band gap. Fig. 6(a) shows a diagram of the corner, edge, and bulk regions in the square-shaped SC. Fig. 6(b) displays the normalized DOS distribution for bulk, edge, and corner states, calculated using Eq. (13), in the frequency range of 5500 Hz to 7900 Hz, with a band gap between 6000 Hz and 7062 Hz. Bulk states dominate wave transmission from 5500 Hz to 6000 Hz and from 7346 Hz to 7900 Hz. Between 7062 Hz and 7346 Hz, edge states overlap with bulk states. In the range from 6000 Hz to 6110 Hz, edge states show the highest DOS, becoming the main mode of sound transmission. Notably, at 6961 Hz, corner states exhibit the highest DOS, serving as the primary mode of acoustic wave propagation.

4. Observation of multi-type corner states in a right-angled trapezoidal sonic crystal

In this section, we investigate the presence of various types of corner states, including those at acute, right, and obtuse angles, within a

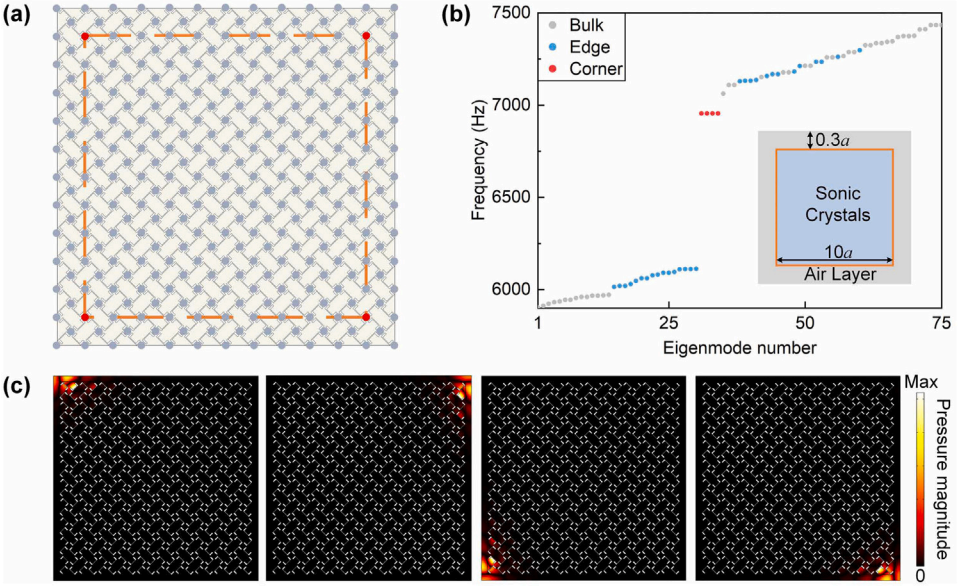

Fig. 5. Bulk spectrum and corner states in the second band gap of the square-shaped SC. (a) Schematic illustration of the finite SC lattice. The gray dots indicate the Wannier center positions, while the red dots indicate the corner states. The orange dashed lines represent the cutting boundaries of the square-shaped SC composed of 10 × 10 unit cells. (b) Bulk spectrum near the second topological band gap for the square-shaped SC surrounded by a 0.3a wide air channel (inset). (c) Sound pressure field distributions of the four corner states with 6962 Hz highlighted in red in panel (b).

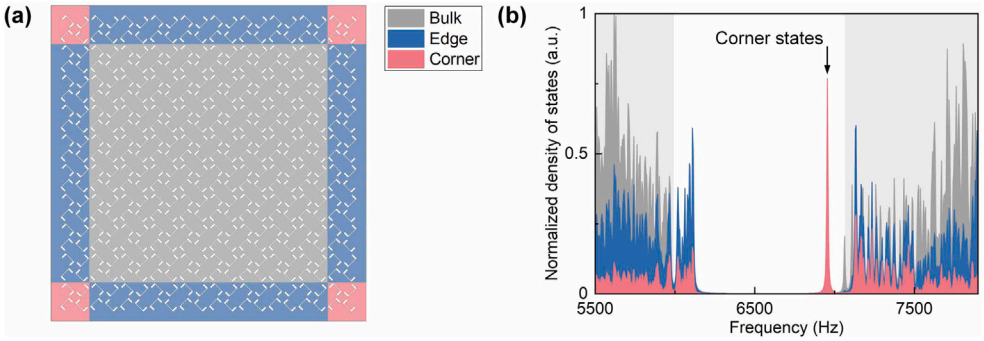

Fig. 6. DOS calculation for the square-shaped SC. (a) Diagram of the corner, edge, and bulk regions in the square-shaped SC, where pink areas indicate corner states, blue areas indicate edge states, and gray areas indicate bulk states. (b) Normalized calculated DOS for bulk, edge, and corner states near the second band gap. Here, a.u. stands for arbitrary units. The white regions represent the band gap areas.

right-angled trapezoidal SC. We identify these corner states through Wannier center analysis, eigenmode analysis, and DOS calculations. To test their robustness, we introduce defects in unit cells near the acute, right, and obtuse angles. We then study the distribution of corner states by adjusting the Wannier center arrangement along the SC boundary, confirming that the presence of corner states is dependent on the Wannier center distribution. Finally, we validate our findings through experimental observations of corner states at different angles in a 3D-printed right-angled trapezoidal SC, supporting our theoretical analysis and calculations.

Fig. 7(a) shows two right-angled trapezoidal SCs (type-I and type-II) with different cutting boundaries, indicated by orange and purple dashed lines. Both structures have a 45° inclination and feature acute, right, and obtuse angles. The cutting boundary of the type-I SC follows the Wannier center, with the Wannier center located at the corners of the SC. As highlighted in previous research [18,46,92,93], when a finite structure is cut along the Wannier centers, it exhibits non-trivial behavior, with second-order corner states likely to appear at the corners, as well as topological edge states at the boundary. This configuration allows for edge states at each boundaries and corner states at each of the corners: acute, right, and obtuse. In contrast, the cutting boundary of the type-II SC does not follow the Wannier center along the hypotenuse edge, and the other three edges have the same cutting boundary as type-I. As a result, the type-II SC has only two right-angled corners with Wannier centers, while the other two corners lack Wannier centers. Thus, the type-II SC has corner states only at the right-angled corners. Additionally, the edge states of the topological quadrupole structure are not affected by the cutting boundaries, so the structure will exhibit edge states similar to those of the type-I SC. The eigenfrequency spectrum near the second band gap of the type-I SC, shown in Fig. 7(b), confirms the presence of corner states. Bulk, edge, and corner states are distinguished by gray, blue, and red dots, respectively. Unlike the square-shaped SC shown in Fig. 5(a), the trapezoidal SC exhibits five distinct corner states and two in-gap hypotenuse edge states (marked by yellow dots). The two right-angled corner states align in frequency with those in the square SC, both occurring at 6962 Hz. The two acute-angled corner states occur at slightly different frequencies — 6963 Hz and 6567 Hz — while the obtuse-angled corner state has a frequency closer to the edge states, appearing at 6164 Hz. The hypotenuse edge states occur at 6718 Hz and 6857 Hz. The sound field distributions for the corner states, hypotenuse edge states, edge state, and bulk state are shown in Fig. 7(d). For the corner states, the sound energy is concentrated at the lattice corners and decays rapidly towards the bulk. In the case of

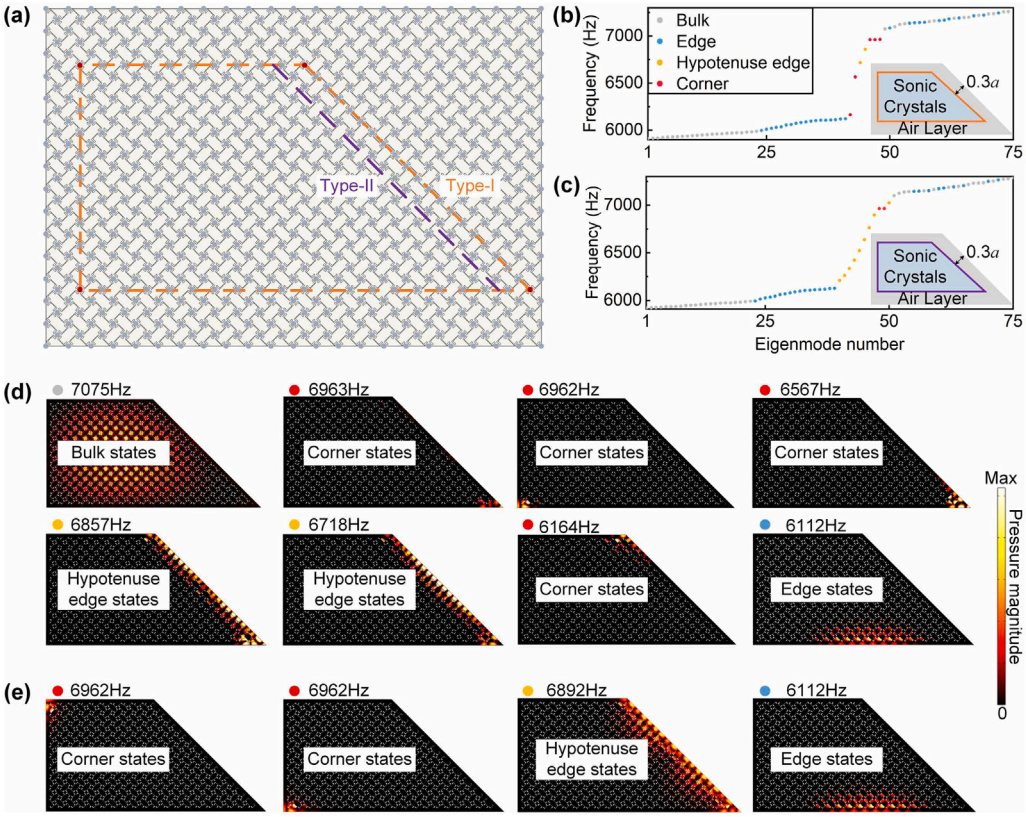

Fig. 7. Bulk spectrum and in-gap eigenmodes within the second band gap of the right-angled trapezoidal SC with different cutting boundaries. (a) Schematic of the finite lattice, where gray dots represent Wannier center positions and red dots indicate corner states. The orange dashed line shows the cutting boundary for the type-I right-angled trapezoidal SC, with an upper base of $10a$, a lower base of $20a$, and a height of $10a$. The purple dashed line represents the cutting boundary for the type-II right-angled trapezoidal SC, where the hypotenuse does not align with the Wannier centers. This type has an upper base of $8.75a$, a lower base of $18.75a$, and a height of $10a$. (b, c) Bulk spectrum near the second topological band gap for the type-I and type-II right-angled trapezoidal SC, surrounded by a $0.3a$ wide air channel (inset), respectively. (d, e) Sound pressure distributions for the corner states, hypotenuse edge states, edge states and bulk state of the type-I and type-II right-angled trapezoidal SC, respectively.

the hypotenuse edge states, the sound pressure field distributions show that most of the acoustic energy is concentrated along the hypotenuse, with some energy extending to the corners. This indicates a mix of edge and corner states. These findings suggest that specific cutting boundaries can lead to the appearance of different eigenmodes. The eigenfrequency spectrum for the type-II SC near the second band gap is shown in Fig. 7(c), where bulk states, edge states, hypotenuse edge states, and corner states are represented by gray, blue, yellow, and red dots, respectively. Unlike the type-I SC, the type-II lattice shows only two right-angled corner states, as shown in Fig. 7(e), but has a larger number of hypotenuse edge states within the band gap.

Based on the analysis and calculation results, it can be concluded that the cutting boundary plays an important role in the formation of corner states. Corner states occur when the Wannier centers are located at the corner points of the SC, with the cutting boundary aligned with these centers. However, if the cutting boundary is not aligned with the Wannier centers and there are no Wannier centers at the corners, the corner states will disappear. This approach can also be applied to other HOTIs.

The DOS spectra for the bulk, edge, and corner states of the type-I SC are calculated using Eq. (13). Fig. 8(a) shows a schematic for calculating the DOS, with the corner states highlighted in pink, edge states in blue, and bulk states in gray. Fig. 8(b) presents the calculated DOS distribution for bulk, edge, and corner states within the frequency range of 5500 Hz to 7900 Hz, with the band gap spanning from 6000 Hz to 7062 Hz. The results show that in the frequency ranges from 5500 Hz to 6000 Hz and 7346 Hz to 7900 Hz, the bulk states dominate as the primary mode of acoustic wave transmission. Between 7062 Hz and 7346 Hz, edge states mix with bulk states. The DOS for edge states peaks between 6000 Hz and 6110 Hz, making them the main modes of sound transmission in this range. Notably, at 6164 Hz, 6567 Hz, and 6961 Hz, corner states show the highest DOS, becoming the dominant mode for acoustic wave transmission.

Then the robustness of the corner states is studied by introducing defects near the associated corners of the unit cell. The unit cells near the acute, right, and obtuse angle corners are rotated counterclockwise by a certain angle to examine how the eigenfrequencies of the corresponding corner states change. Considering that when the rotation angle exceeds 8°, portions of the scatterers extend beyond their original unit cell boundaries, the rotation angle is intentionally limited to $\leq 8°$ to maintain structural integrity. For the acute-angle corner, when the unit cell is rotated counterclockwise by 0-8° (Fig. 9(a)), the eigenfrequencies of the corner states shift slightly downward. After 8° of rotation, the frequencies of the two acute-angle states are 6520 Hz and 6952 Hz, which represent only small shifts of 0.6% and 0.1%, respectively, compared to the unrotated frequencies of 6563 Hz and 6960 Hz. Additionally, the sound pressure field distribution shown in Fig. 9(a) remains nearly unchanged. Similarly, when the unit cell near the obtuse-angle corner is rotated counterclockwise by 0-8° (Fig. 9(b)), the eigenfrequency of the obtuse-angle corner state shifts slightly upward. After 8° of rotation, the obtuse-angle frequency is 6227 Hz, which represents a small shift of 0.9% from the unrotated frequency of 6164 Hz. The sound pressure field distribution changes only minimally. For the right-angle corner state, the behavior is slightly different. As the rotation increases from 0 to 8°, the eigenfrequency gradually shifts upward and eventually enters the bulk acoustic band (Fig. 9(c)). After 8° of rotation, the frequency is 7095 Hz, compared to 6959 Hz in the unrotated state, showing a 1.9% shift. The sound pressure field extends

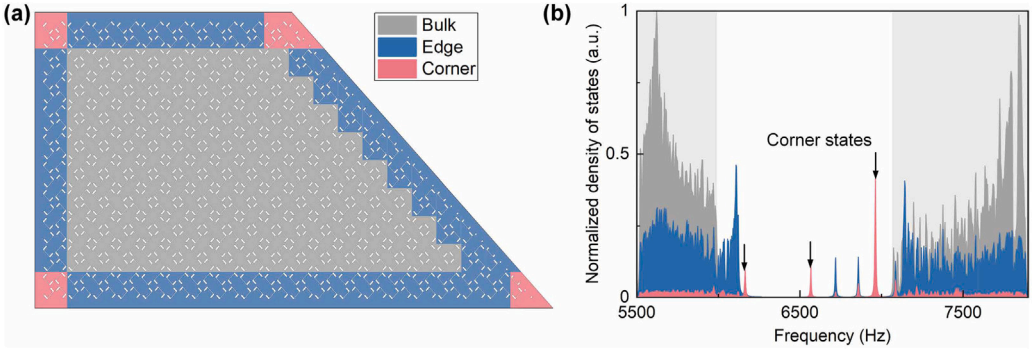

Fig. 8. DOS for the right-angled trapezoidal SC. (a) Diagram of the corner, edge, and bulk regions in the right-angled trapezoidal SC, where pink areas indicate corner states, blue areas indicate edge states, and gray areas indicate bulk states. (b) Normalized calculated DOS for bulk, edge, and corner states near the second band gap of the right-angled trapezoidal SC. The black arrows indicate the corner states.

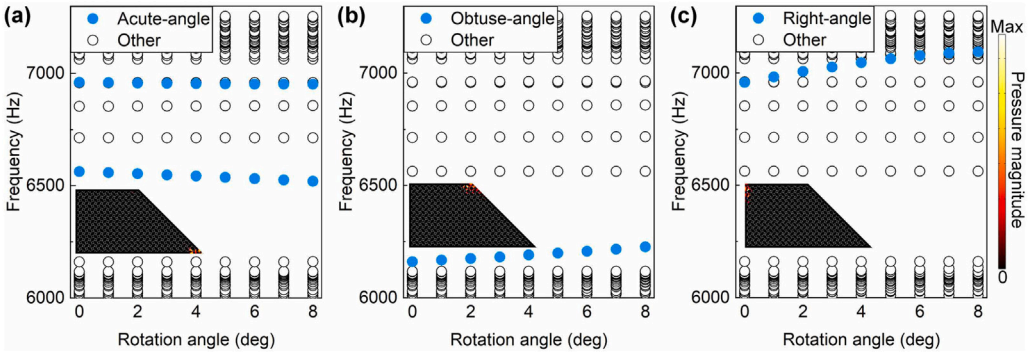

Fig. 9. The robustness of corner states in the right-angled trapezoidal SC. Changes in eigenfrequency of the corner states after rotating the unit cells by 0-8° counterclockwise for (a) acute-angle, (b) obtuse-angle, and (c) right-angle corner states. The insets in the figure show the distribution of the sound pressure field in each corner state after rotated by 8°.

slightly towards the edge. Based on the frequency deviations calculated above, it appears that rotational defects have the least impact on acute-angled corner states, followed by obtuse-angled corner states, with the largest effect on right-angled corner states. However, in general, the frequency deviations for all three corner states are relatively small (< 2%), indicating that the corner states are robust to this type of defect.

To experimentally validate the presence of various types of corner states, a right-angled trapezoidal type-I SC is constructed from photosensitive resin using a 3D printer, as shown in Fig. 10(a). In the experimental setup, the lattice is placed on a bottom plate, sealed with an acrylic plate on top, and surrounded by acrylic plates, effectively forming a 2D waveguide for the experiment. To minimize background noise interference, the experiment is carried out in an anechoic room. To simulate a point source, a 2-mm-radius circular hole is drilled at the bottom of each corner (port) of the sample. A tin foil cylinder (2 mm radius) is connected between the speaker (BOACH-Test-SS-S30) and these holes: one end attaches to the speaker outlet, and the other to the hole at the port. To measure signals at other corners, 2-mm holes are drilled into the acrylic plate above each port. A 1/4-inch microphone (BSWA-MFF14) is inserted into each hole, with gaps sealed using rubber cement to prevent sound leakage. To verify edge states, the speaker at Port 2 emits white noise (6–8 kHz). Sound intensity signals at Ports 1, 3, and 4 are recorded. Within the second topological bandgap frequency range, signals transmitted from Port 2 to Ports 1, 3 propagate exclusively via edge states, while signals at Port 4 reflect bulk states (as no bandgap transmission from Port 2 to Port 4). The signals obtained from ports 1 and 3 indicate the presence of edge states, while the signal from port 4 depict the bulk state. These sound intensity signals are then forwarded to a PC for post-processing through a data acquisition card (BOACH-Test-D.R-DRH12). Fig. 10(b) shows the sound intensity spectra of acoustic waves through the right-angled trapezoidal sample, with signals from ports 1, 3, and 4 shown as blue, yellow, and red curves, respectively. In the gray regions, the sound intensity collected from port 4 is similar to that from the other ports, indicating that sound waves can travel through the intermediate sample from port 2 to port 4, representing acoustic pass bands. Within the white region in the middle, certain signals from ports 1 and 3 are considerably higher than those from port 4, suggesting that sound waves only propagate along the boundaries of the SC, not through the intermediate region. This indicates that the white region corresponds to a band gap spanning from 6240 Hz to 7810 Hz. The difference between the measured band gap and the calculated frequency is mainly due to the following reasons. On the one hand, the discrepancies between the measured and calculated results are primarily due to fabrication errors during sample preparation. Specifically, thermal stress during the printing process, along with the large sample size, cause some warping at the bottom surface of the printed sample. Additionally, the outer frame of the trapezoidal structure do not fit perfectly with the sample, contributing to the differences observed. On the other hand, temperature and humidity effects on sound speed also play a role.

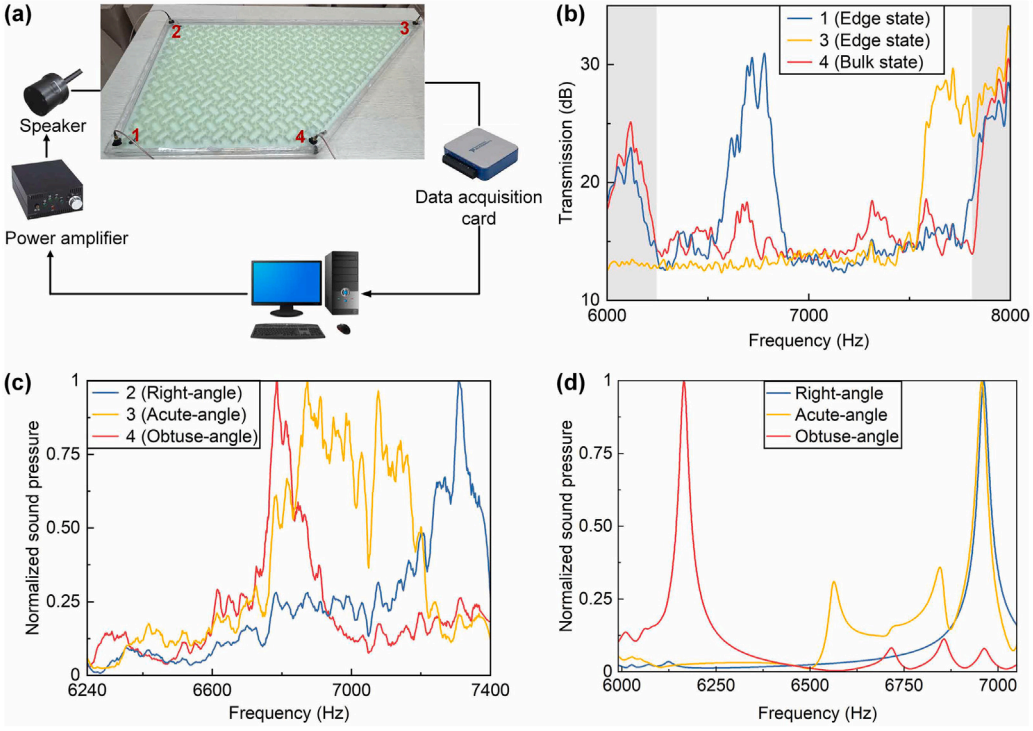

Fig. 10. Experiment testing of the right-angled trapezoidal sample. (a) Schematic of experimental process. Points 1, 2, 3, and 4 stand for the sound wave input and receive port. (b) Experimentally measured sound intensity spectra at ports 1, 3, and 4 with the sound source placed at port 2. (c) Normalized sound pressure spectra measured at ports 2 (right-angle corner state), 3 (acute-angle corner state), and 4 (obtuse-angle corner state) when the sound source is placed at the same port for each measurement (d) Simulated transmission spectra for the acute, obtuse, and right-angle corner states in the SC with a loss factor $\eta = 0.002$.

Theoretical calculations typically assume a standard sound speed of 343 m/s at 20 °C, but variations in lab conditions, such as temperature fluctuations or changes in humidity, can alter the actual sound speed.

The sound source is sequentially placed at ports 2, 3, and 4, and excited within the frequency range of 6240 Hz to 7400 Hz to capture the signals characteristic of different types of corner states. The collected signals are normalized to ensure that all three peak values reach unity, as shown in Fig. 10(c). The signals from ports 2, 3, and 4 are represented by blue, yellow, and red curves, corresponding to right-angle, acute-angle, and obtuse-angle corner states, respectively. The frequencies at which these signals occur are 6784 Hz (obtuse-angle), 6873 Hz (acute-angle), 7077 Hz (acute-angle), and 7310 Hz (right-angle). Notably, the acute-angle state shows a broader frequency range, which can be attributed to the influence of the hypotenuse edge states. These edge states overlap with the acute-angle states, resulting in an additional peak in the acoustic signal and broadening the frequency range of the acute-angle state. This behavior matches the simulated transmission spectrum shown in Fig. 10(d). To account for environmental losses, we set the sound velocity to $c = 343(1 + \eta\,\mathrm{i})$ m/s, where η is the loss factor, with $\eta = 0.002$ used, and additional loss factors are provided in Appendix B. The spectra are normalized for comparison, with the peak values as the reference. The acute-angle state (yellow curve) shows three peaks at 6566 Hz, 6857 Hz, and 6964 Hz. The 6857 Hz peak corresponds to a mode formed by the coupling of the hypotenuse and acute-angle states, as shown in Fig. 7(c). This mode causes a non-negligible sound field at the acute angle, leading to the additional peak. The obtuse-angle state (red curve) peaks at 6164 Hz, near the frequency of the edge states, while the right-angle state (blue curve) peaks at 6963 Hz. Overall, the experimental results confirm the presence of three distinct types of corner states in the right-angled trapezoidal SC, with frequency distributions that match theoretical predictions.

5. Conclusion

In conclusion, this work demonstrates multi-type topological corner states enabled by C-shaped square-lattice unit cells with $p4gg$ symmetry. The glide symmetry induces acoustic band sticking effects along the XM and YM lines. The topological nature of the second band gap is confirmed through Wannier band and nested Wannier band calculations, revealing gapped, non-degenerate Wannier bands due to glide symmetry protection. The presence of corner states is validated by analyzing the topological quadrupole index of 1/2, derived from the nested Wannier bands and further supported by the locations of Wannier centers predicted from the acoustic modes at high-symmetry points. Wannier center distributions are systematically utilized to characterize and predict these corner states in lattices of generalized geometries.

The key innovation of this study lies in the realization of multi-type corner states (including non-right-angle states) within a trapezoidal topological SC, leveraging the glide-symmetric topological quadrupole. The unique distribution of corner states at right, obtuse, and acute angles, each occurring at different frequencies, enabling independent excitation— a critical feature absent in prior studies where corner states are degenerate. Additionally, this specific boundary cutting generates the in-gap hypotenuse edge states, which is a combination of edge and corner states. More importantly, altering the cutting boundary of the SC changes the distribution of Wannier centers at the boundaries and corners of the SC, thus affecting the existence of corner states. Finally, we systematically examine damping effects. Through simulations, we find that corner states maintain spatial localization under moderate damping. Additionally, as the loss factor increases, the peak width of corner states broadens, indicating reduced energy localization.

These findings hold significant implications for the design and application of topological SC. By fabricating a 3D-printed right-angled

trapezoidal SC, we experimentally verify the existence of diverse corner states. This approach offers new possibilities for the precise control and manipulation of acoustic waves, potentially enabling advanced acoustic devices and applications based on topological phenomena.

CRediT authorship contribution statement

Tao Yang: Writing – review & editing, Writing – original draft, Validation, Software, Methodology, Formal analysis, Conceptualization. **Qian Wu:** Writing – review & editing, Validation, Methodology, Formal analysis. **Shaoyun Wang:** Methodology, Formal analysis. **Rongyao Wei:** Software, Investigation. **Yu Liu:** Software, Investigation. **Quan Wang:** Writing – review & editing, Validation. **Heng Jiang:** Writing – review & editing, Supervision, Funding acquisition. **Guoliang Huang:** Writing – review & editing, Supervision, Methodology, Formal analysis.

Declaration of competing interest

The authors declare that they have no known competing financial interests or personal relationships that could have appeared to influence the work reported in this paper.

Acknowledgments

This work is supported by the National Natural Science Foundation of China (Grant No. 12372144) and the Beijing Municipal Natural Science Foundation (Grant No. L245006).

Appendix A. Calculation process of nested wannier bands

First, the lattice cell is discretized into a 100 × 100 grid, as shown in Fig. A.1(a). Since the sound field is primarily distributed within the air medium, points within the scatterers are excluded. The BZ is subsequently discretized into a 30 × 30 grid, as shown in Fig. A.1(b). Since the boundary of the BZ is periodic, only one edge in the k_x- and k_y-directions is chosen to be discrete. Floquet periodic boundary conditions are applied to all four edges of the unit cell, and the Pressure Acoustics module in COMSOL is used to compute the characteristic sound field distribution for each wave vector. Using the coordinates $\boldsymbol{r}$ and the calculated acoustic pressure field $|P_{n,\boldsymbol{k}}\rangle$ at each point, the acoustic wave function $|u_{n,\boldsymbol{k}}\rangle$ is derived based on Eq. (1). This generates the acoustic wave function matrix for the entire unit cell under each wave vector, which is then used to compute the Wilson loop operator matrix.

The calculation process for the Wilson loop operator is illustrated in Fig. A.2, where the red and blue paths represent the Wilson loops in the x- and y-directions, respectively. Using k_x as an example, we select (k_x, k_y) as the starting point and follow the red path to traverse the BZ. Each segment of the Wilson loop is defined by the inner product of the acoustic wave functions at neighboring wave vectors, $\left\langle u_{m,\boldsymbol{k}+\Delta k_x} \mid u_{n,\boldsymbol{k}} \right\rangle$. By sequentially connecting these segments, we construct the complete Wilson loop around (k_x, k_y). Applying this process across the BZ enables us to obtain the Wannier band of the lattice cell. For the calculation of the nested Wannier bands within the second topological band gap, two primary paths are followed, as shown in Fig. A.2. In the first path, we first compute a Wilson loop along the k_x-direction, $W_{x,(k_x+\frac{2\pi}{a},k_y)\leftarrow(k_x,k_y)}$ (indicated in red), and then along the k_y-direction, $\tilde{W}_{y,(k_x,k_y+\frac{2\pi}{a})\leftarrow(k_x,k_y)}$ (indicated in blue). The second path begins with a Wilson loop in the k_y-direction, $W_{y,(k_x,k_y+\frac{2\pi}{a})\leftarrow(k_x,k_y)}$ (blue), followed by one in the k_x-direction, $\tilde{W}_{x,(k_x+\frac{2\pi}{a},k_y)\leftarrow(k_x,k_y)}$ (red). Due to the $p4gg$ symmetry of the unit cell, both paths yield consistent results for the Wannier bands and nested Wannier bands.

Appendix B. Influence of the loss factor on transmission spectra

To simulate the transmission spectrum of the experimental corner states, we account for environmental losses by setting the sound velocity to $c = 343(1 + \eta\,\mathrm{i})$ m/s, where η represents the loss factor. The corner states are excited by their corresponding sources, and the transmission spectra are measured between 6000 Hz and 7050 Hz. The transmission spectra for the acute, obtuse, and right-angled corner states in the right-angled trapezoidal SC with varying loss factors are shown in Fig. B.1. The figure displays clear peak signals for the acute, right, and obtuse corner states at loss factors $\eta = 0.001$ and 0.005. Specifically, the acute-angle corner state shows three distinct peaks at 6566 Hz, 6857 Hz, and 6964 Hz. The 6857 Hz peak in the acute-angle spectrum corresponds to a mode formed by the coupling of the hypotenuse and acute-angle states. As the loss factor increases, the peak width broadens. The energy of corner states spreads across multiple frequencies and not concentrated at a single frequency, indicating reduced energy localization.

Appendix C. Determination of the wannier center distribution within the unit cell

Based on the results of the nested Wilson loop calculation and considering the $p4gg$ symmetry, there are two types of Wannier center distributions within unit cell, shown in Fig. C.1. To further determine

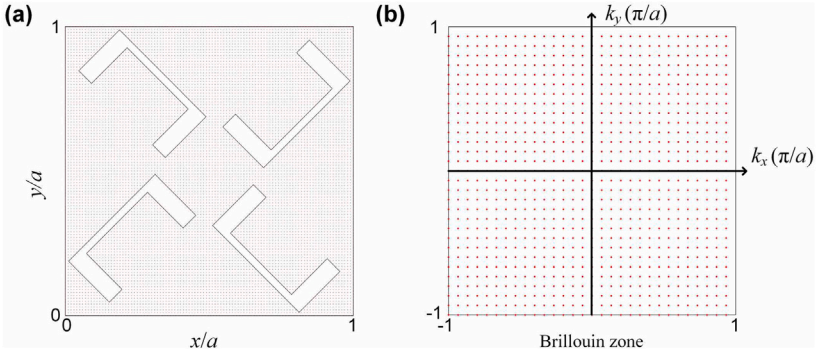

Fig. A.1. Discretization. Discretization of (a) the unit cell and (b) BZ. The red dots denote the meshing grid points.

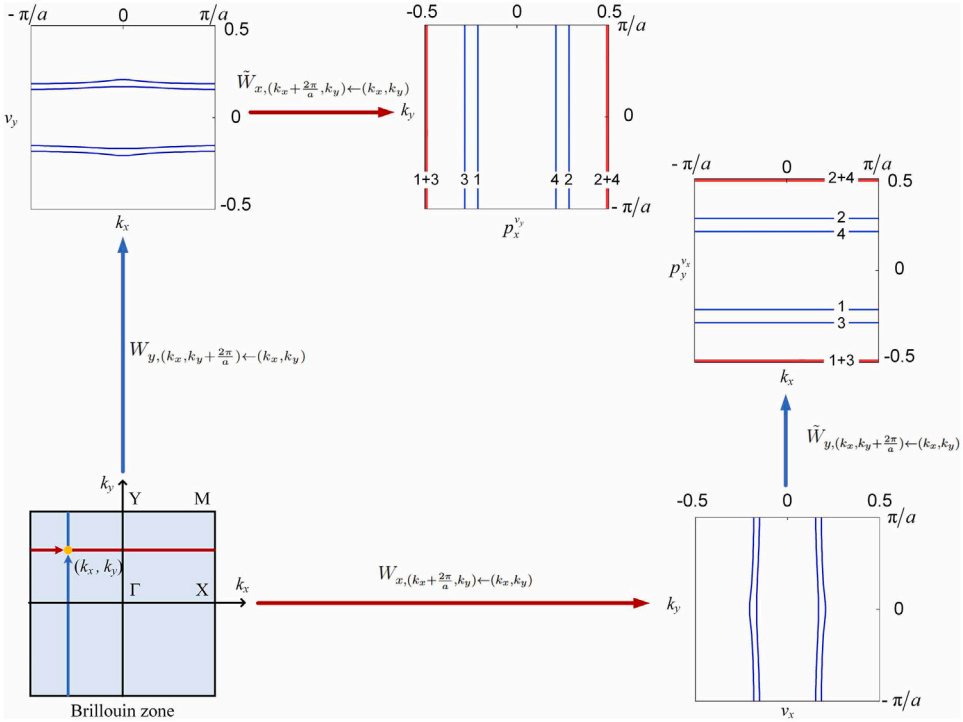

Fig. A.2. Calculation process of the nested Wannier bands for the second topological band gap. The process is divided into two paths: one calculates the Wilson loop along the k_x direction, $W_{x,(k_x+\frac{2\pi}{a},k_y)\leftarrow(k_x,k_y)}(k_y)$, followed by a Wilson loop in the k_y direction, $\tilde{W}_{y,(k_x,k_x+\frac{2\pi}{a})\leftarrow(k_x,k_y)}(k_x)$; the other calculates the Wilson loop along the k_y direction, $W_{y,(k_x,k_y+\frac{2\pi}{a})\leftarrow(k_x,k_y)}(k_x)$, followed by a Wilson loop in the k_x direction, $\tilde{W}_{x,(k_x+\frac{2\pi}{a},k_y)\leftarrow(k_x,k_y)}(k_y)$.

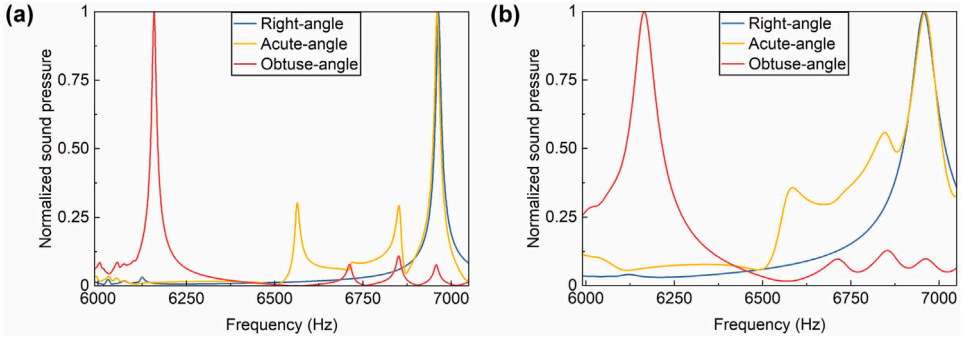

Fig. B.1. Influence of loss factor on transmission spectra. Transmission spectra for the acute, obtuse, and right-angle corner states in the SC with a loss factor (a) $\eta = 0.001$; (b) $\eta = 0.005$. The yellow, red, and blue curves correspond to the acute, obtuse, and right-angle corner states, respectively.

the exact distribution of the Wannier centers, it is necessary to analyze their eigenmodes. The position of the Wannier center must also comply with the glide symmetry operation, which introduces a nontrivial phase factor (i and -i). As a result, for Fig. C.1(b), this leads to the parity eigenvalues of the wavefunctions at the X and Y points being opposite parities. However, for Fig. C.1(a), there is no such effect at the X and Y points. Therefore, it is sufficient to analyze the eigenmodes at the X, Y, and M points. Therefore, the Wannier center configuration can be determined simply by analyzing the eigenmodes at the high symmetry points X, Y and M. Based on the eigenmode in Fig. 3, it can be seen that the parities at points X, Y are the same, and therefore the Wannier center of the structure is distributed at the points M and Γ.

Appendix D. Topological corner states with different widths of air channel

The width of the channel affects the existence of topological edge states and corner states. We calculate the acoustic channels with different widths, ranging from $0.2a$ to $0.4a$, as shown in Fig. D.1. As the width of the air channel decreases, the corner states gradually merge with the bulk modes, making them harder to observe. Specifically, when the channel width is $0.2a$, the corner states even disappear. For a channel width of $0.4a$, the obtuse-angle corner states are not observable, and the bulk spectrum only shows four corner state frequencies — two for the right-angle corner states and two for the acute-angle corner states — where the two right-angle corner states are excited

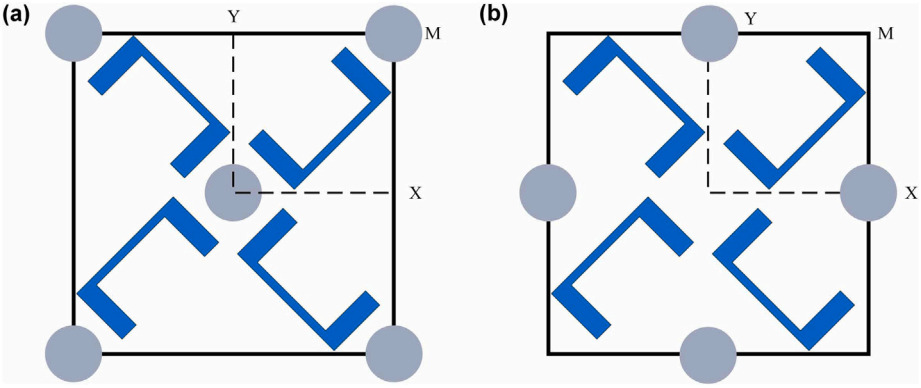

Fig. C.1. Two types of Wannier centers within the unit cell. (a) The Wannier center is located at the center of the unit cell and at the four corner points, the high symmetry points Γ and M; (b) The Wannier center is positioned at the midpoints of the four edges of the unit cell, the high symmetry points X and Y..

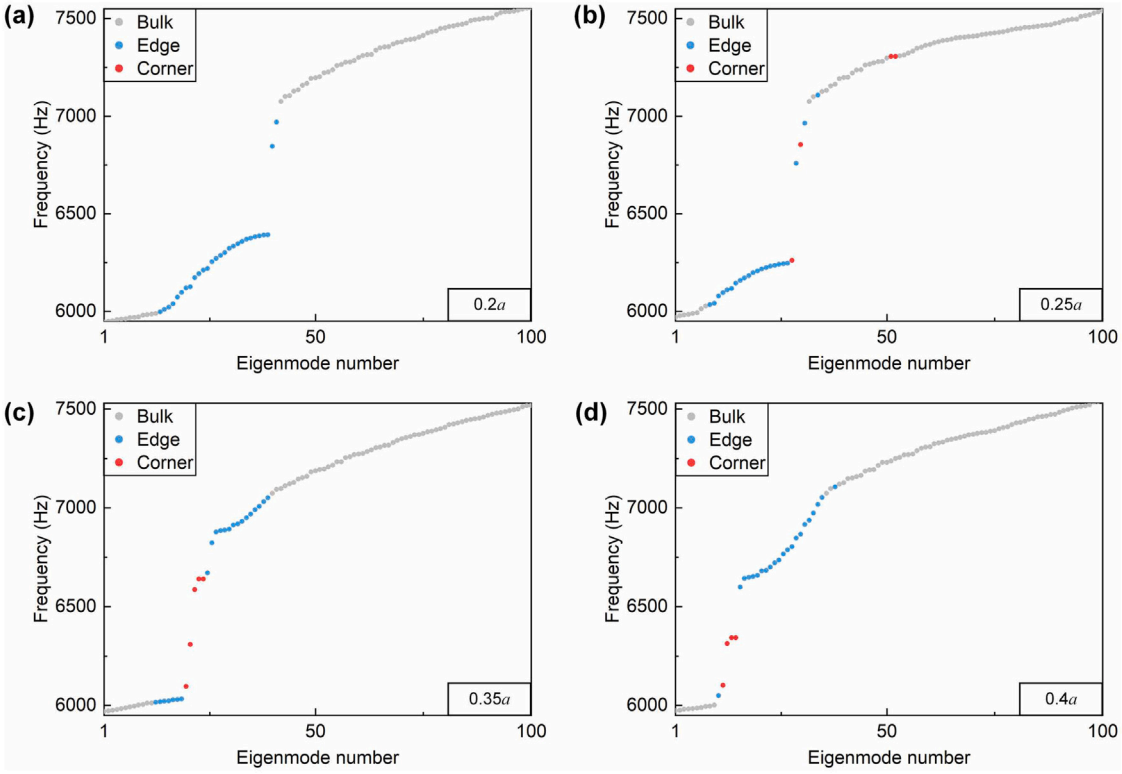

Fig. D.1. Bulk spectrum of the right-angle trapezoidal SC with different acoustic channel widths. (a) 0.2a; (b) 0.25a; (c) 0.35a; (d) 0.4a..

simultaneously. Therefore, a channel width of 0.3a or 0.35a is more suitable for observing the corner states. To facilitate experimental measurement, we chose a channel width of 0.3a.

Appendix E. Topological corner states analysis of trapezoidal SC

The observation of five distinct corner states in the trapezoidal SC primarily arises from the splitting of corner states at the acute-angled vertex. As illustrated in Fig. E.1, the acoustic field patterns reveal that the two corner states at the acute-angled vertex exhibit distinct symmetries: one adopts a symmetric mode along the central axis of the acute angle, while the other displays an antisymmetric mode. This splitting originates from the non-uniform spacing of Wannier center distributions along the two intersecting boundaries at the acute-angled corner. Such spatial disparity creates distinct effective potential fields for the corner states, thereby enabling the emergence of two discrete corner states. In contrast, while the Wannier center distributions at the obtuse-angled corner also exhibit spatial variation, the larger angular opening of the obtuse angle diminishes the localized influence of this spacing disparity. Consequently, the potential field homogenizes across the broader angular region, resulting in a single corner state at the obtuse-angled vertex. This asymmetry in boundary confinement effects between acute and obtuse angles underpins the observed imbalance in corner state multiplicity.

Furthermore, we study the differences between corner states in square and trapezoidal SCs as follows:

Square SC: Identical geometric environments at all four right-angle corners induce uniform Wannier center spacing along intersecting

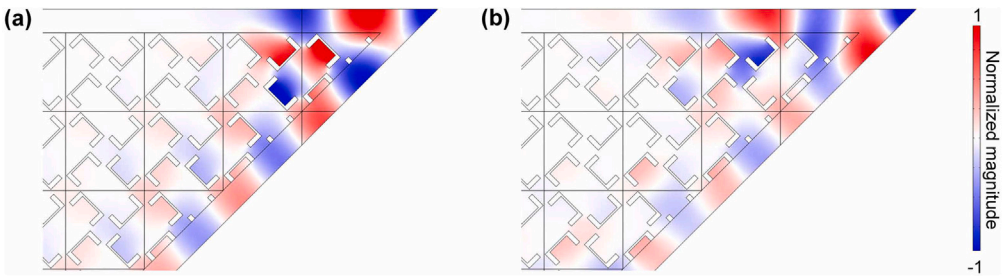

Fig. E.1. Two types of corner states at acute angle. (a) Symmetric mode, the acoustic field exhibit symmetric mode along the central axis of the acute angle; (b) Antisymmetric mode.the acoustic field exhibit antisymmetric mode along the central axis of the acute angle.

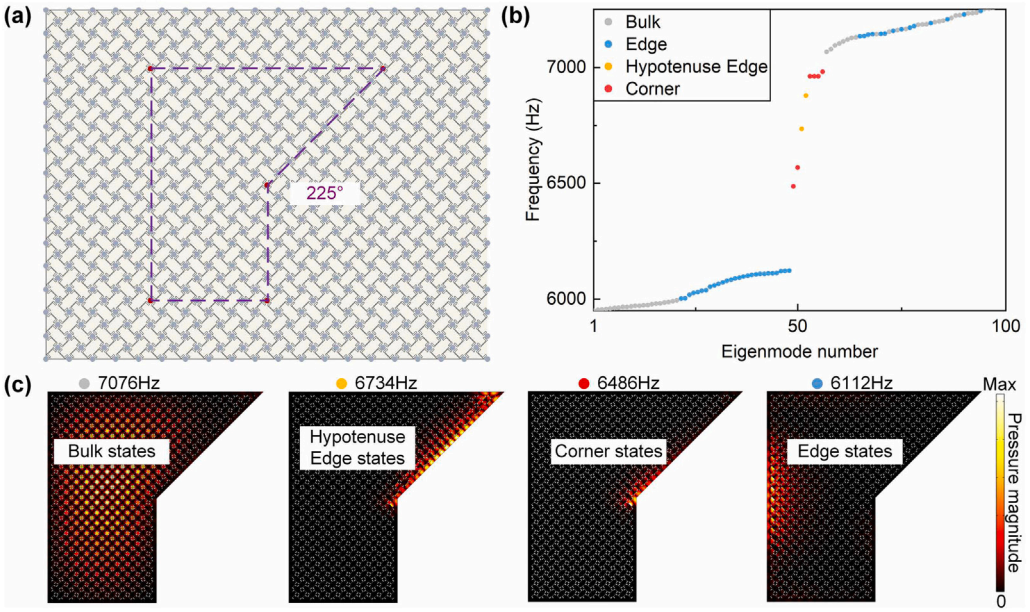

Fig. F.1. Bulk spectrum and in-gap eigenmodes within the second band gap of the polygonal SC containing a 225° angle. (a) Schematic of the finite lattice. (b) Bulk spectrum near the second topological band gap for the SC, surrounded by a 0.3a wide air channel. (c) Sound pressure distributions for the corner states, hypotenuse edge states, edge states and bulk state of the SC,.

boundaries. This spatial homogeneity creates degenerate corner states with identical eigenfrequencies. The preserved p4gg symmetry enforces robust topological protection, rendering corner states highly localized and resistant to perturbations.

Trapezoidal SC: Different geometric shapes at the acute, right, and obtuse angle corners lead to non-degenerate corner states. The distribution of Wannier centers on the two boundaries that form these corners is not the same, which results in different effective potential fields for the corner states. As a result, these corner states are non-degenerate and can be excited independently. Reduced symmetry lifts degeneracy but enables angle-tunable state engineering—a feature absent in square lattices.

Appendix F. Corner states in general geometry

We take a step forward by exploring irregular lattices that incorporate both conventional right angles and non-right angles, including those exceeding 180° (see Fig. F.1, F.2, and F.3). We construct polygonal SCs with three different angles: 225°, 270°, and 315°. The boundaries of these lattices are all cut along the Wannier centers, ensuring that Wannier centers are distributed at the boundaries and corner points. Based on the Wannier center characterization of corner states, we observe that corner states also occur in all angles larger than 180°, with frequencies of 6486 Hz, 6330 Hz and 6194 Hz, respectively, and it can be found that the frequency decreases with the increase of the angle. From the bulk spectrum, it can be seen that the frequency of all the three SC right-angle corner states remains constant at 6962 Hz. In addition, the distribution of the sound field of their corner states can be seen that the energy of the sound field is localized in the vicinity of the angular point. Furthermore, these corner states are non-degenerate and can be excited individually. We have calculated the robustness of these corner states by rotating the lattice cells near the corner point counterclockwise by 1–8 degrees. The frequency shifts of the corner states are shown in Fig. F.4, and it is evident that the frequencies remain largely unchanged during the rotation process, indicating their high robustness.

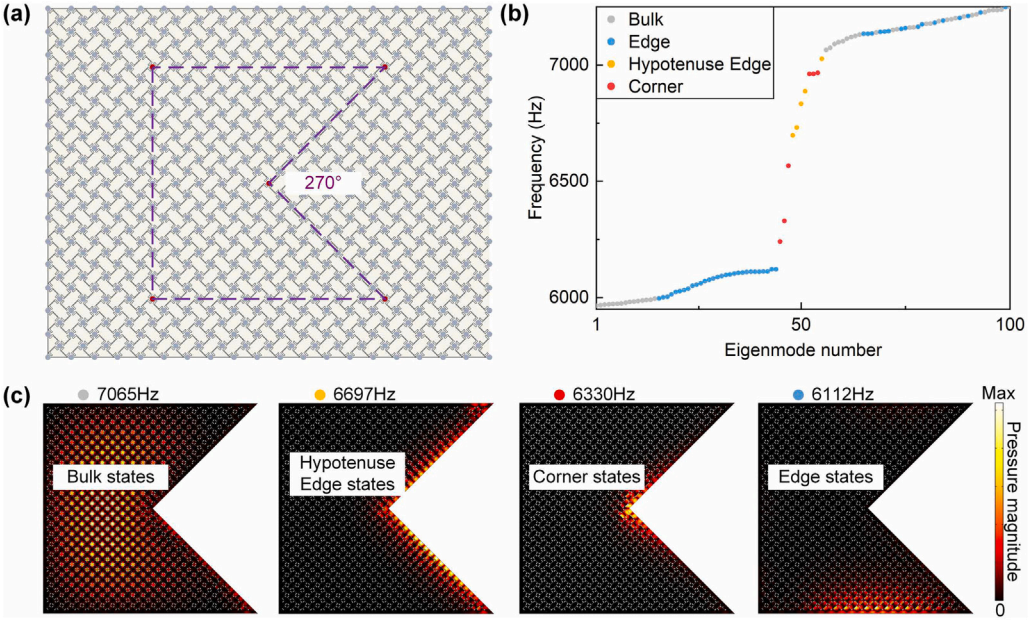

Fig. F.2. Bulk spectrum and in-gap eigenmodes within the second band gap of the polygonal SC containing a 270° angle. (a) Schematic of the finite lattice. (b) Bulk spectrum near the second topological band gap for the SC, surrounded by a 0.3a wide air channel. (c) Sound pressure distributions for the corner states, hypotenuse edge states, edge states and bulk state of the SC,.

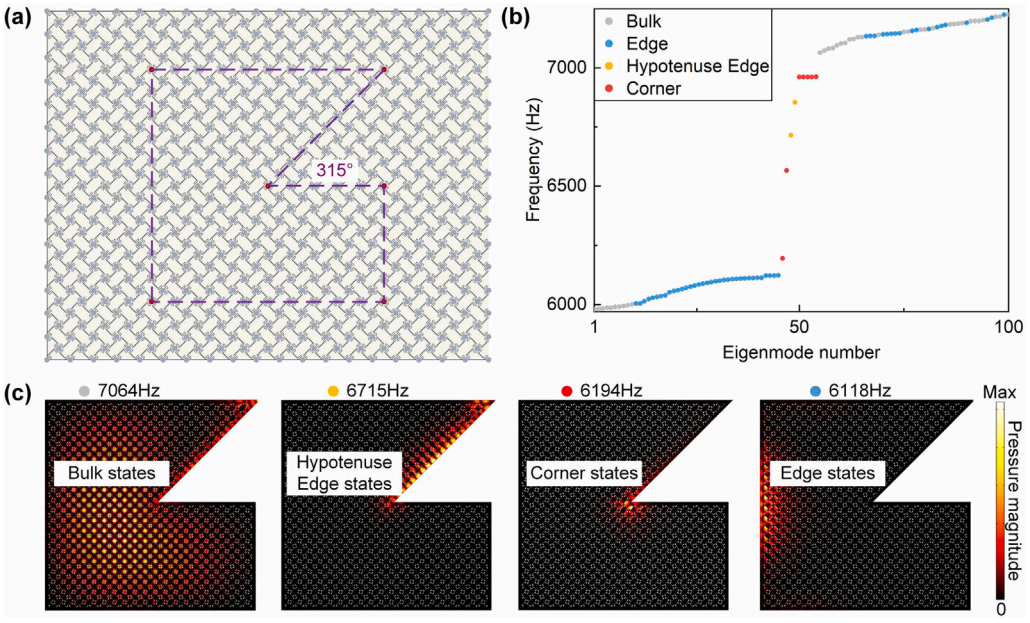

Fig. F.3. Bulk spectrum and in-gap eigenmodes within the second band gap of the polygonal SC containing a 315° angle. (a) Schematic of the finite lattice. (b) Bulk spectrum near the second topological band gap for the SC, surrounded by a 0.3a wide air channel. (c) Sound pressure distributions for the corner states, hypotenuse edge states, edge states and bulk state of the SC,.

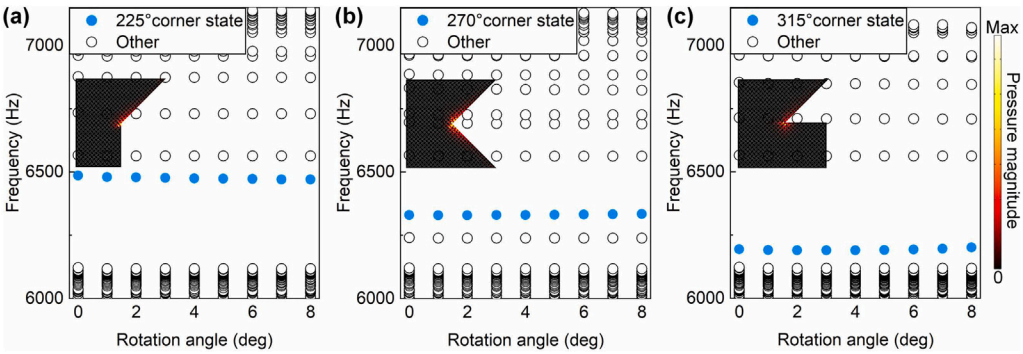

Fig. F.4. The robustness of corner states in the polygonal SC containing angles greater than 180°. Changes in eigenfrequency of the corner states after rotating the unit cells by 0-8° counterclockwise for (a) 225° angle, (b) 270° angle, and (c) 315° angle corner states. The insets in the figure show the distribution of the sound pressure field in each corner state after rotated by 8°.

Data availability

Data will be made available on request.

References

[1] Klitzing Kv, Dorda G, Pepper M. New method for high-accuracy determination of the fine-structure constant based on quantized Hall resistance. Phys Rev Lett 1980;45(6):494.

[2] Hasan MZ, Kane CL. Colloquium: topological insulators. Rev Modern Phys 2010;82(4):3045–67.

[3] Cage ME, Klitzing K, Chang A, Duncan F, Haldane M, Laughlin RB, et al. The quantum Hall effect. Springer Science & Business Media; 2012.

[4] Zhang Y, Tan Y-W, Stormer HL, Kim P. Experimental observation of the quantum Hall effect and Berry's phase in graphene. Nature 2005;438(7065):201–4.

[5] Bernevig BA, Zhang S-C. Quantum spin Hall effect. Phys Rev Lett 2006;96(10):106802.

[6] Bernevig BA, Hughes TL, Zhang S-C. Quantum spin Hall effect and topological phase transition in HgTe quantum wells. Science 2006;314(5806):1757–61.

[7] Mak KF, McGill KL, Park J, McEuen PL. The valley Hall effect in MoS2 transistors. Science 2014;344(6191):1489–92.

[8] Marino E, Nascimento LO, Alves VS, Smith CM. Interaction induced quantum valley Hall effect in graphene. Phys Rev X 2015;5(1):011040.

[9] Chen Z-G, Xu C, Al Jahdali R, Mei J, Wu Y. Corner states in a second-order acoustic topological insulator as bound states in the continuum. Phys Rev B 2019;100(7):075120.

[10] Liu Z. Trapping sound at corners. Nat Mater 2019;18(2):98–9.

[11] Peterson CW, Benalcazar WA, Hughes TL, Bahl G. A quantized microwave quadrupole insulator with topologically protected corner states. Nature 2018;555(7696):346–50.

[12] Schindler F, Cook AM, Vergniory MG, Wang Z, Parkin SS, Bernevig BA, Neupert T. Higher-order topological insulators. Sci Adv 2018;4(6):eaat0346.

[13] Xie B, Wang H-X, Zhang X, Zhan P, Jiang J-H, Lu M, et al. Higher-order band topology. Nat Rev Phys 2021;3(7):520–32.

[14] Ni X, Li M, Weiner M, Alù A, Khanikaev AB. Demonstration of a quantized acoustic octupole topological insulator. Nat Commun 2020;11(1):2108.

[15] Benalcazar WA, Bernevig BA, Hughes TL. Quantized electric multipole insulators. Science 2017;357(6346):61–6.

[16] Luo X-J, Wu F. Generalization of Benalcazar-Bernevig-Hughes model to arbitrary dimensions. Phys Rev B 2023;108(7):075143.

[17] Yin J-X, Lian B, Hasan MZ. Topological Kagome magnets and superconductors. Nature 2022;612(7941):647–57.

[18] Xue H, Yang Y, Gao F, Chong Y, Zhang B. Acoustic higher-order topological insulator on a Kagome lattice. Nat Mater 2019;18(2):108–12.

[19] Chen C, Chen T, Ding W, Zhang R, Zhu J. Acoustic higher-order topological states in Kagome lattice with split-ring resonators. Int J Mech Sci 2024;265:108903.

[20] Fleury R, Khanikaev AB, Alu A. Floquet topological insulators for sound. Nat Commun 2016;7(1):11744.

[21] Peng Y-G, Qin C-Z, Zhao D-G, Shen Y-X, Xu X-Y, Bao M, et al. Experimental demonstration of anomalous Floquet topological insulator for sound. Nat Commun 2016;7(1):13368.

[22] Xie B, Liu H, Cheng H, Liu Z, Chen S, Tian J. Acoustic topological transport and refraction in a Kekulé lattice. Phys Rev Appl 2019;11(4):044086.

[23] Zhang C-x, Chen A, Hu W, Yang J, Liang B, Christensen J, et al. Topological heterostructures for spectrally nearly constant intensity enhancements of audio sound and ultrasonics. Phys Rev Appl 2023;20(2):024040.

[24] Hu B, Zhang Z, Zhang H, Zheng L, Xiong W, Yue Z, et al. Non-Hermitian topological whispering gallery. Nature 2021;597(7878):655–9.

[25] Gu Z, Gao H, Liu T, Liang S, An S, Li Y, et al. Topologically protected exceptional point with local non-Hermitian modulation in an acoustic crystal. Phys Rev Appl 2021;15(1):014025.

[26] Zhang Z, Tian Y, Wang Y, Gao S, Cheng Y, Liu X, et al. Directional acoustic antennas based on valley-hall topological insulators. Adv Mater 2018;30(36):1803229.

[27] Zheng S, Duan G, Xia B. Underwater acoustic positioning based on valley-chirality locked beam of sonic system. Int J Mech Sci 2020;174:105463.

[28] Ma C, Wu JH, Cui Z, Wang L. Topological acoustic waveguide with high-precision internal-mode-induced multiband. Compos Struct 2024;327:117681.

[29] Mousavi SH, Khanikaev AB, Wang Z. Topologically protected elastic waves in phononic metamaterials. Nat Commun 2015;6(1):8682.

[30] Zheng L-Y, Christensen J. Three-dimensional quantum Hall effect in acoustic crystals. Sci Bull 2024;69(14):2149–50.

[31] Zhang X, Wei Q, Peng M, Deng W, Lu J, Huang X, et al. Observation of 3D acoustic quantum Hall states. Sci Bull 2024.

[32] Chen H, Yao L, Nassar H, Huang G. Mechanical quantum Hall effect in time-modulated elastic materials. Phys Rev Appl 2019;11(4):044029.

[33] He C, Ni X, Ge H, Sun X-C, Chen Y-B, Lu M-H, et al. Acoustic topological insulator and robust one-way sound transport. Nat Phys 2016;12(12):1124–9.

[34] Sun X-C, Chen H, Lai H-S, Xia C-H, He C, Chen Y-F. Ideal acoustic quantum spin Hall phase in a multi-topology platform. Nat Commun 2023;14(1):952.

[35] Zhang Z, Wei Q, Cheng Y, Zhang T, Wu D, Liu X. Topological creation of acoustic pseudospin multipoles in a flow-free symmetry-broken metamaterial lattice. Phys Rev Lett 2017;118(8):084303.

[36] Liu P, Li H, Zhou Z, Pei Y. Topological acoustic tweezer and pseudo-spin states of acoustic topological insulators. Appl Phys Lett 2022;120(22).

[37] Lu J, Qiu C, Ye L, Fan X, Ke M, Zhang F, et al. Observation of topological valley transport of sound in sonic crystals. Nat Phys 2017;13(4):369–74.

[38] Wu Z, Xia R, Yi J, Li Z. Multiple topological interface modes in electromechanically resonant piezoelectric beams. Eng Struct 2023;281:115716.

[39] Xu J, Zheng Y, Ma T, Chen H, Wu B, Wang J, et al. Realization of topological valley Hall edge states of elastic waves in phononic crystals based on material differences. Phys Rev Appl 2023;19(3):034062.

[40] Liang X, Zhang Z, Chu J, Luo J, Meng D, Zhou Z. Acoustic valley Hall topological insulators with controllable band gap. Mater Today Commun 2024;38:107755.

[41] Wu Z, Chen J, Wang W, Xu J, Shao S, Xia R, et al. Elastic wave demultiplexer with frequency dependent topological valley Hall edge states. Thin-Walled Struct 2024;201:111997.

[42] Wu Q, Wang S, Qian H, Wang Y, Huang G. Understanding of topological mode and skin mode morphing in 1D and 2D non-Hermitian resonance-based meta-lattices. J Mech Phys Solids 2024;105907.

[43] Tian Y, Tan Z, Zhang W. Hermitian and non-Hermitian higher-order topological states in mechanical metamaterials. Eur J Mech A Solids 2024;106:105294.

[44] Gao H, Xue H, Gu Z, Liu T, Zhu J, Zhang B. Non-hermitian route to higher-order topology in an acoustic crystal. Nat Commun 2021;12(1):1888.

[45] Zhang X, Tian Y, Jiang J-H, Lu M-H, Chen Y-F. Observation of higher-order non-Hermitian skin effect. Nat Commun 2021;12(1):5377.

[46] Ni X, Weiner M, Alu A, Khanikaev AB. Observation of higher-order topological acoustic states protected by generalized chiral symmetry. Nat Mater 2019;18(2):113–20.

[47] Qi Y, Qiu C, Xiao M, He H, Ke M, Liu Z. Acoustic realization of quadrupole topological insulators. Phys Rev Lett 2020;124(20):206601.

[48] Xie B-Y, Wang H-F, Wang H-X, Zhu X-Y, Jiang J-H, Lu M-H, et al. Second-order photonic topological insulator with corner states. Phys Rev B 2018;98(20):205147.

[49] Wu Q, Chen H, Li X, Huang G. In-plane second-order topologically protected states in elastic Kagome lattices. Phys Rev Appl 2020;14(1):014084.
[50] Serra-Garcia M, Peri V, Süsstrunk R, Bilal OR, Larsen T, Villanueva LG, et al. Observation of a phononic quadrupole topological insulator. Nature 2018;555(7696):342–5.
[51] Duan G, Zheng S, Xia B. Multi-dimensional wave manipulation with 3D mechanical higher-order topological insulators. Int J Mech Sci 2024;265:108890.
[52] Zhang G, Yan W, Gao Y. Higher-order elastic topological insulators with reconfigurable route and tunable corner states. Int J Mech Sci 2024;264:108820.
[53] Long J, Wang A, Zhou Y, Chen CQ. Quadrupole higher-order topological phases in static mechanical metamaterials. Int J Mech Sci 2024;263:108782.
[54] Du Z, Luo J, Xu Z, Jiang Z, Ding X, Cui T, et al. Higher-order topological insulators by ML-enhanced topology optimization. Int J Mech Sci 2023;255:108441.
[55] Yi J, Chen CQ. Delocalization and higher-order topology in a nonlinear elastic lattice. New J Phys 2024;26(6):063004.
[56] Zheng Z, Yin J, Wen J, Yu D. Higher-order topological states in locally resonant elastic metamaterials. Appl Phys Lett 2022;120(14).
[57] Duan G, Zheng S, Lin Z-K, Jiao J, Liu J, Jiang Z, et al. Numerical and experimental investigation of second-order mechanical topological insulators. J Mech Phys Solids 2023;174:105251.
[58] Zheng S, Man X, Kong Z-L, Lin Z-K, Duan G, Chen N, et al. Observation of fractal higher-order topological states in acoustic metamaterials. Sci Bull 2022;67(20):2069–75.
[59] Li Y, Qiu H, Zhang Q, Qiu C. Acoustic higher-order topological insulators protected by multipole chiral numbers. Phys Rev B 2023;108(20):205135.
[60] Wu S-Q, Lin Z-K, Xiong Z, Jiang B, Jiang J-H. Square-root higher-order topology in rectangular-lattice acoustic metamaterials. Phys Rev Appl 2023;19(2):024023.
[61] Geng Z-G, Shen Y-X, Xiong Z, Duan L, Chen Z, Zhu X-F. Quartic-root higher-order topological insulators on decorated three-dimensional sonic crystals. APL Mater 2024;12(2).
[62] Yan M, Huang X, Luo L, Lu J, Deng W, Liu Z. Acoustic square-root topological states. Phys Rev B 2020;102(18):180102.
[63] Wang S, Hu Z, Wu Q, Chen H, Prodan E, Zhu R, et al. Smart patterning for topological pumping of elastic surface waves. Sci Adv 2023;9(30):eadh4310.
[64] Chen H, Zhang H, Wu Q, Huang Y, Nguyen H, Prodan E, et al. Creating synthetic spaces for higher-order topological sound transport. Nat Commun 2021;12(1):5028.
[65] Chen Z-G, Zhu W, Tan Y, Wang L, Ma G. Acoustic realization of a four-dimensional higher-order Chern insulator and boundary-modes engineering. Phys Rev X 2021;11(1):011016.
[66] Liu H, Wang H, Xie B, Cheng H, Liu Z, Chen S. Acoustic corner state transfer mapping to synthetic higher-order topological semimetal. Phys Rev B 2023;108(16):L161104.
[67] Zhang X, Wang H-X, Lin Z-K, Tian Y, Xie B, Lu M-H, et al. Second-order topology and multidimensional topological transitions in sonic crystals. Nat Phys 2019;15(6):582–8.
[68] Li H, Wang Z, Wang Z, Liu Z, Zhang X, Luo J, et al. Experimental observation of the multiple higher-order extensible topological states in acoustic systems. Phys Rev Appl 2022;18(4):044050.
[69] Wu Y, Yan M, Lin Z-K, Wang H-X, Li F, Jiang J-H. On-chip higher-order topological micromechanical metamaterials. Sci Bull 2021;66(19):1959–66.
[70] Xiong Z, Lin Z-K, Wang H-X, Zhang X, Lu M-H, Chen Y-F, et al. Corner states and topological transitions in two-dimensional higher-order topological sonic crystals with inversion symmetry. Phys Rev B 2020;102(12):125144.
[71] Wang Z, Wei Q, Xu H-Y, Wu D-J. A higher-order topological insulator with wide bandgaps in Lamb-wave systems. J Appl Phys 2020;127(7).
[72] Meng F, Chen Y, Li W, Jia B, Huang X. Realization of multidimensional sound propagation in 3D acoustic higher-order topological insulator. Appl Phys Lett 2020;117(15).
[73] Weiner M, Ni X, Li M, Alù A, Khanikaev AB. Demonstration of a third-order hierarchy of topological states in a three-dimensional acoustic metamaterial. Sci Adv 2020;6(13):eaay4166.
[74] Zhang X, Xie B-Y, Wang H-F, Xu X, Tian Y, Jiang J-H, et al. Dimensional hierarchy of higher-order topology in three-dimensional sonic crystals. Nat Commun 2019;10(1):5331.
[75] Wei Q, Zhang X, Deng W, Lu J, Huang X, Yan M, et al. 3D hinge transport in acoustic higher-order topological insulators. Phys Rev Lett 2021;127(25):255501.
[76] Huo S-y, Huang H-b, Feng L-y, Chen J-j. Edge states and corner modes in second-order topological phononic crystal plates. Appl Phys Express 2019;12(9):094003.
[77] Chen C-W, Chaunsali R, Christensen J, Theocharis G, Yang J. Corner states in a second-order mechanical topological insulator. Commun Mater 2021;2(1):62.
[78] Wu S-Q, Lin Z-K, Jiang B, Zhou X, Hang ZH, Hou B, et al. Higher-order topological states in acoustic twisted Moiré superlattices. Phys Rev Appl 2022;17(3):034061.
[79] Košata J, Zilberberg O. Second-order topological modes in two-dimensional continuous media. Phys Rev Res 2021;3(3):L032029.
[80] Yu X, Zhang X, Luo L, Wang L, Peng J, Huang Y, et al. Acoustic transport in higher-order topological insulators with Dirac hierarchy. New J Phys 2023;25(6):063008.
[81] Fan H, Xia B, Tong L, Zheng S, Yu D. Elastic higher-order topological insulator with topologically protected corner states. Phys Rev Lett 2019;122(20):204301.
[82] Zhang Z, Long H, Liu C, Shao C, Cheng Y, Liu X, et al. Deep-subwavelength holey acoustic second-order topological insulators. Adv Mater 2019;31(49):1904682.
[83] Ma Z, Liu Y, Xie Y-X, Wang Y-S. Tuning of higher-order topological corner states in a honeycomb elastic plate. Phys Rev Appl 2023;19(5):054038.
[84] Zhu W, Xue H, Gong J, Chong Y, Zhang B. Time-periodic corner states from Floquet higher-order topology. Nat Commun 2022;13(1):11.
[85] Wang Z, Li H, Wang Z, Liu Z, Luo J, Huang J, et al. Straight-angled corner state in acoustic second-order topological insulator. Phys Rev B 2021;104(16):L161401.
[86] Zhang X, Lin Z-K, Wang H-X, Xiong Z, Tian Y, Lu M-H, et al. Symmetry-protected hierarchy of anomalous multipole topological band gaps in nonsymmorphic metacrystals. Nat Commun 2020;11(1):65.
[87] Benalcazar WA, Bernevig BA, Hughes TL. Electric multipole moments, topological multipole moment pumping, and chiral hinge states in crystalline insulators. Phys Rev B 2017;96(24):245115.
[88] Lin Z-K, Wang H-X, Xiong Z, Lu M-H, Jiang J-H. Anomalous quadrupole topological insulators in two-dimensional nonsymmorphic sonic crystals. Phys Rev B 2020;102(3):035105.
[89] Wang H-X, Guo G-Y, Jiang J-H. Band topology in classical waves: Wilson-loop approach to topological numbers and fragile topology. New J Phys 2019;21(9):093029.
[90] Bradlyn B, Elcoro L, Cano J, Vergniory MG, Wang Z, Felser C, et al. Topological quantum chemistry. Nature 2017;547(7663):298–305.
[91] Liu Z, Zhou X, Wei G, Gao L, Hou B, Xiao J-J. Topological corner modes by composite Wannier states in glide-symmetric photonic crystal. Laser Photon Rev 2024;2300783.
[92] Ezawa M. Minimal models for Wannier-type higher-order topological insulators and phosphorene. Phys Rev B 2018;98(4):045125.
[93] Ezawa M. Higher-order topological insulators and semimetals on the breathing Kagome and pyrochlore lattices. Phys Rev Lett 2018;120(2):026801.